A Drop Size Distribution (DSD)-Based Model for Evaluating the Performance of Wet Radomes for Dual-Polarized Radars

Jorge L. Salazar-Cerreño*

Advanced Study Program, National Center for Atmospheric Research,[+] Boulder, Colorado

V. Chandrasekar

Department of Electrical and Computer Engineering, Colorado State University, Fort Collins, Colorado

Jorge M. Trabal, Paul Siquera, Rafael Medina, Eric Knapp, and David J. McLaughlin

Department of Electrical and Computer Engineering, University of Massachusetts Amherst, Amherst, Massachusetts

ABSTRACT

A novel analytical method is presented for evaluating the electrical performance of a radome for a dual-polarized phased-array antenna under rain conditions. Attenuation, reflections, and induced cross polarization are evaluated for different rainfall conditions and radome types. The authors present a model for estimating the drop size distribution on a radome surface based on skin surface material, area, inclination, and rainfall rate. Then, a multilayer radome model based on the transmission-line-equivalent circuit model is used to characterize the radome's scattering parameters. Numerical results are compared with radar data obtained in the Next Generation Weather Radar (NEXRAD) and Collaborative Adaptive Sensing of the Atmosphere (CASA) systems, and good agreement is found.

1. Introduction

In general, any radome should provide electromagnetic transparency and structural strength to protect the antenna. Electromagnetic transparency consists of low reflections, low transmission loss, and minimum distortion of polarization-dependent antenna patterns. Structural strength is related to wind loading, stability, and integrity for mitigating environmental conditions, such as temperature, humidity, and pressure. For operational systems, the radome is the essential component, since it minimizes the high wind load, reduces the need for a heavy and expensive pedestal, provides consistent nominal temperatures that facilitate the operation and maintenance, and improves the life cycle cost of the system (Walton 1970). One adverse effect of the radome is the performance degradation of radio signals when they operate in the presence of water or ice. Water accumulated on the radome surface can significantly affect the radar signal. Depending on the frequency of operation, rain and wind conditions, shape, and material, a radome can significantly attenuate, reflect, and depolarize the radar or communication signals.

For frequencies below S band, the impact of wet radomes is relatively small and cannot be considered critical for radar operation (see Table 1). However, for higher frequencies water formation on the radome surface can significantly deteriorate the transmit and receive signals. The attenuation of radio signals on satellite systems that operate between 17 and 22 GHz has been extensively analyzed in the past regarding the large attenuation in the radio signals caused by water accumulation on the radome surface (Gibble 1964; Blevis 1965; Cohen and Smolski 1966; Anderson 1975; Hendrix et al. 1989; Chang 1985; Fenn 1997; Crane 2002).

Before the existence of repellent materials, the attenuation of a wet radome was evaluated based on the

* Current affiliation: Advanced Radar Research Center, University of Oklahoma, Norman, Oklahoma.

[+] The National Center for Atmospheric Research is sponsored by the National Science Foundation.

Corresponding author address: Jorge L. Salazar-Cerreño, 3190 Monitor Ave., Radar Innovation Laboratory, RIL-110, Norman, OK 73079.
E-mail: salazar@ou.edu

TABLE 1. Reported transmission losses in wet radome in atmospheric radars.

Band	Rain rate ($mm\,h^{-1}$)	Two-way attenuation (dB)		Condition	References
		Standard	Hydrophobic		
20 GHz	05		2.0	Artificial rain	Fenn (1997)
	10	14.2	2.2	Artificial rain	Chang (1985)
	10	14.4	3.6	Theory/measured	Chang (1985)
	20	15.0	4.8	Theory/measured	Chang (1985)
	40	—	5.0	Theory/measured	Chang (1985)
	50	16.2	4.2	Artificial rain	Fenn (1997)
	60	16.4	5.2	Theory/measured	Chang (1985)
	80	16.8	5.4	Theory/measured	Chang (1985)
	100	18.0	5.6	Theory/measured	Chang (1985)
	160		5.8	Theory/measured	Chang (1985)
X	10	2.9	—	Theory	Frasier et al. (2013)
	10	4.40	2.1	Measured	Frasier et al. (2013)
	10	6.40	3.1	Artificial rain	Bechini et al. (2010)
	10	7.40	1.8	Measured	Trabal et al. (2008)
	25	8.90	4.8–4.9	Measured	Gorgucci et al. (2013)
	40		0.50	Artificial rain	SCAT (2009)
	100		0.60	Artificial rain	SCAT (2009)
	200		0.65	Artificial rain	SCAT (2009)
	300		0.65	Artificial rain	SCAT (2009)
C	10	4.0	0.50	Theory	Manz et al. (1999)
	15	5.0	0.80	Laboratory and simulations	Effenberger et al. (1986)
	22.1	9.5	3.9 ± 1.5	Laboratory and artificial, clean	Kurri and Huuskonen (2008)
	22.1	19	4.3 ± 1.4	Laboratory and artificial, dirty	Kurri and Huuskonen (2008)
	100		3.32	Theory	Merceret and Ward (2002)
	200		6.63	Theory	Merceret and Ward (2002)
	300		5.00	Artificial rain	Manz et al. (1999)
S	15	2.00	0.3	Laboratory and simulations	Effenberger et al. (1986)
	10	1.50	0.3	Theory	Manz et al. (1999)
	20	0.56	0.2	Theory	Merceret and Ward (2002)
	100	2.80	0.98	Theory	Merceret and Ward (2002)
	200	5.60	1.95	Theory	Merceret and Ward (2002)

water layer thickness using Gibble's formulation (Gibble 1964; Blevis 1965), which assumes that formation of water on a radome consists of a thin film of water. Later experimental results by Anderson (1975) and Chang (1985) show a significant difference between their experimental results and theoretical results based on a laminar flow model proposed by Gibble (1964). Anderson's results suggest the discrepancies could be attributed to two factors. A laminar flow model assumes a continuous uniform film of water forming on the radome surface, which occurs in heavy rain conditions. The second factor can be the fact that in time the radome surface can accumulate a thin film of grime (pollution, dirt, sand, etc.) that can change the wettability characteristic of the radome surface, inducing rivulet and film formation.

Hendrix et al. (1989) evaluated the depolarization effect of the wet radome using two unweathered radome materials, ESCOLAM-6 and ESCOLAM-8. The study reveals that ESCOLAM-8 presents hydrophobic properties and causes less attenuation, and that the presence of film water and rivulets degrades the cross-polarization signals. Later, Fenn (1997) conducted measurements to evaluate the attenuation and depolarization of a hydrophobic air-supported radome in artificial rain. Results indicate that a substantial depolarization effect is due to the presence of droplets and rivulets on the radome surface. Fenn's study found cross-polarization degradation from −34 (dry radome) to −33, −30, and −27 dB for rain rates of 5, 10, and 50 mm h^{-1}, respectively.

Hydrophobic surfaces have the capability to repel water from the surface and minimize film water and the formation of rivulets. For this reason, most antenna radomes for meteorological and communication applications include nonwetting or hydrophobic materials on the radome surface to mitigate the effect of the rain on the radar's performance. To evaluate and characterize the wet radome performance, experimental measurements are the most reliable method of determining the signal attenuation in a radar or communication system. In addition to Chang (1985), Hendrix et al. (1989), Fenn (1997), and Merceret and Ward (2002) proposed an
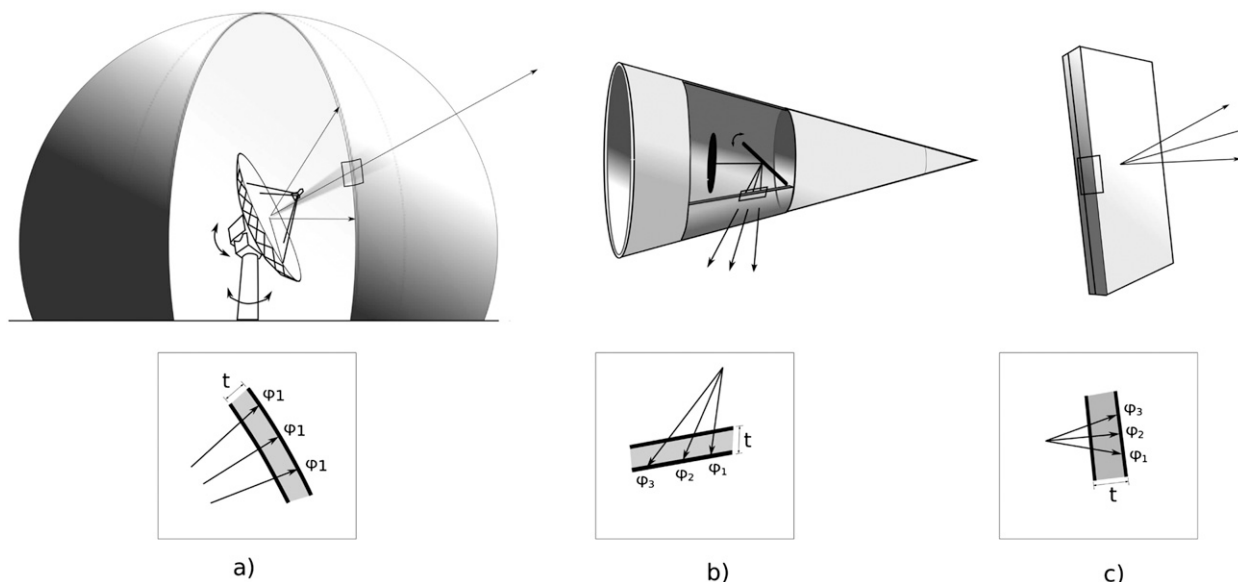
FIG. 1. Common radar shapes: (a) semispherical radome, (b) conical airborne radome, and (c) flat phased-array radome.

empirical formulation to estimate the two-way losses of a hydrophobic radome as a function of the rainfall rate, frequency, and a constant that depends on the hydrophobic material used. The computed two-way losses for S- and C-band radars indicate an improvement factor of 3 in two-way attenuation when a hydrophobic coating is added on the radome surface.

Dual-polarized radars require high-polarization isolation and a high degree of matched beam patterns (for H and V) (Bringi and Chandrasekar 2001). An accurate calibration procedure that includes the adverse effect of the wet radome is required to accurately estimate precipitation rate and to better classify hydrometeors (Gorgucci et al. 1992). Observations in previous references indicate that rivulet formation can significantly affect the vertical channel more than the horizontal channel due to the vertical patterns. The radar calibration process should be maintained constantly during radar operation to satisfy those requirements and to achieve accurate radar data. To fully characterize the attenuation effect of a wet radome, experimental radome measurements and a computational simulation are commonly used. Further, such an experimental method can provide a better understanding of the physical phenomena required in addition to the radome: expensive radio frequency (RF) equipment (disdrometer, network analyzer, generators, and well-calibrated antennas) and enough space to create artificial rain and deploy the experiment. An example of an experimental estimation of attenuation by a wet X-band radome is presented by Bechini et al. (2010). In their study, a two-way loss of 12–14 dB for artificial rain of $156 \pm 58 \, \mathrm{mm \, h^{-1}}$ over the cylindrical

radome surface was reported. In this specific experiment, a high uncertainty regarding the artificial rain intensity $(\pm 58 \, \mathrm{mm \, h^{-1}})$ is attributed to the small size of the sprinkler and to wind present during the experiment.

A study that investigated the behavior of a wet radome in polarimetric moments was conducted by Frech (2009). Data from C-band radar with a 12-yr-old orange peel radome were statistically analyzed. The largest impact was identified for Z_{DR}, where a bias higher than 0.8 dB was reported for a rainfall rate between 2 and $22 \, \mathrm{mm \, h^{-1}}$. A study that quantifies the impact of the polarimetric measurements of a wet radome was reported by Gorgucci et al. (2013). Gorgucci proposed a new real-time calibration technique that takes into account the losses induced by the wet radome. The real-time calibration method was validated using the empirical model proposed by Bechini et al. (2010) and also by a comparison between the rain gauges' data. An extended Kalman filter (EKF) algorithm capable of radome and rain attenuation correction was proposed by Schneebeli et al. (2012). The proposed EKF algorithm was used for a polarimetric X-band radar data, and the results suggest that the correction of radome attenuation should become part of the standard radar data processing scheme. Another way to correct the wet radome attenuation of X-band radars is through direct comparison of observations made by two radars, one with a radome and the other without a radome (Trabal et al. 2008; Frasier et al. 2013; Thompson et al. 2012).

Most previous studies were either experimental or parameterized based on rain rate. However, past

experimental studies show that radome attenuation is not just dependent on rainfall rate, but there is quite a bit of variability due the different drop size distribution can be generated depending of the radome skin material condition. In this paper we present a new analytical model that considers the full drop size distribution (DSD) and models the radome performance based on the DSD of rainfall. To validate this model, a numerical simulation and experimental data obtained in radome samples under rain were compared. In addition, radar data obtained from the Weather Surveillance Radar-1988 Doppler (WSR-88D) and the Collaborative Adaptive Sensing of the Atmosphere (CASA) radar were compared.

2. Background

Radomes are designed to minimize attenuation and reflection. Depending on the application, frequency, and technology, the radome can be designed in different shapes. A spherical radome is preferred for ground-based communication and radar systems. These provide full symmetry and less distortion as a function of angle. Quantitative information about the adverse effect of the antenna patterns on the spherical radome joint scattering signals in three radome types (quasi random, orange peel, and igloo) was introduced by Manz et al. (1999). Later, Frech et al. (2013) presents a study of one radar site with three source sites to do the antenna pattern measurements. The study shows a small influence of the radome (dry conditions) in the antenna patterns (copolar and cross polar). Small (but negligible) degradation of the radome the radar moments were also found.

A quasi-random-type radome does not show a preferred scattering direction, which can provide lower perturbation in the antenna patterns, especially in the sidelobe performance. A conical antenna is suitable for airborne radar applications; the typical conical radome requires a rigid structure (a sandwich wall type) to support mechanical stress at high altitude. Thick walls and asymmetry with respect to the antenna can create angle-dependent attenuation and phase distortion. A flat radome is suitable for phased-array antenna applications. Similar to the conical radome, the flat radome presents angle-dependent distortion in amplitude and phase. Figure 1 is a graphic representation of the spherical, conical, and flat radome structures. The figure also illustrates the phase differences of the projected thickness due to the angular position of the signals with respect to the source position. In the case of a conical or flat radome, the attenuation, reflection, and depolarization are angular dependent.
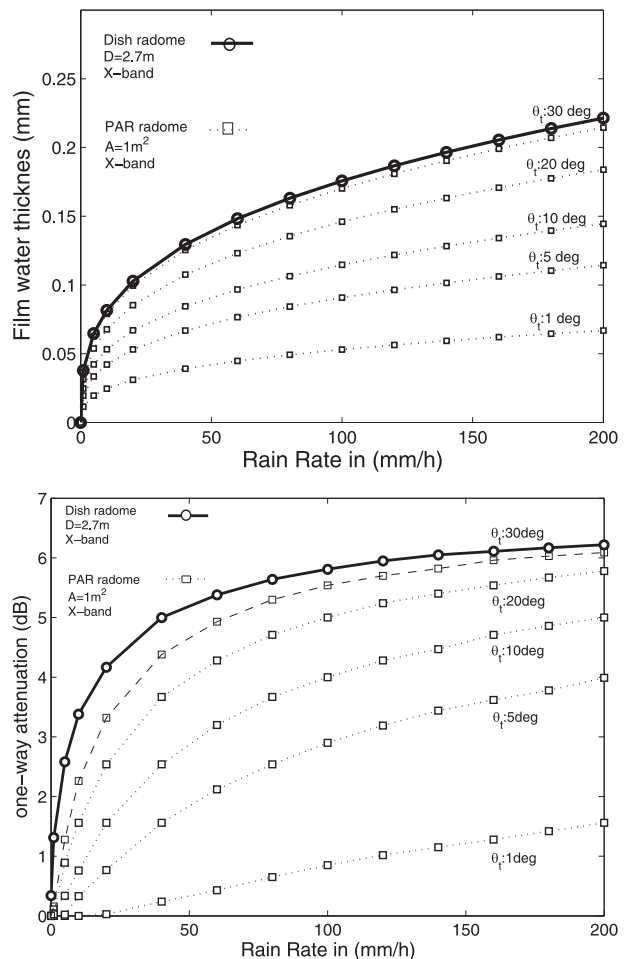

FIG. 2. Comparison of thickness of the water film and the rain-induced attenuation on a spherical radome vs on a planar array (nonhydrophobic); both at X band.

An accurate estimation of rain rate based on polarimetric radar requires a high degree of matching between dual-polarized far-field patterns (principally in the main beam) and near sidelobes. Dual-polarized radar parameters are sensitive to pattern distortion and polarization isolation (Bringi and Chandrasekar 2001).

In the presence of heavy rain, water accumulated over the radar radome and the surrounding rain can significantly attenuate the radar signal to the point of completely extinguishing it (Trabal et al. 2008; SCAT 2009). The relationship between rain intensity and the thickness of a water film formed over the radome without repellent treatment was mathematically modeled by Gibble (1964). The thickness of the mass flow of fluid moving along a semispherical radome can be estimated using Gibble's Eq. (10), presented in Anderson (1975),
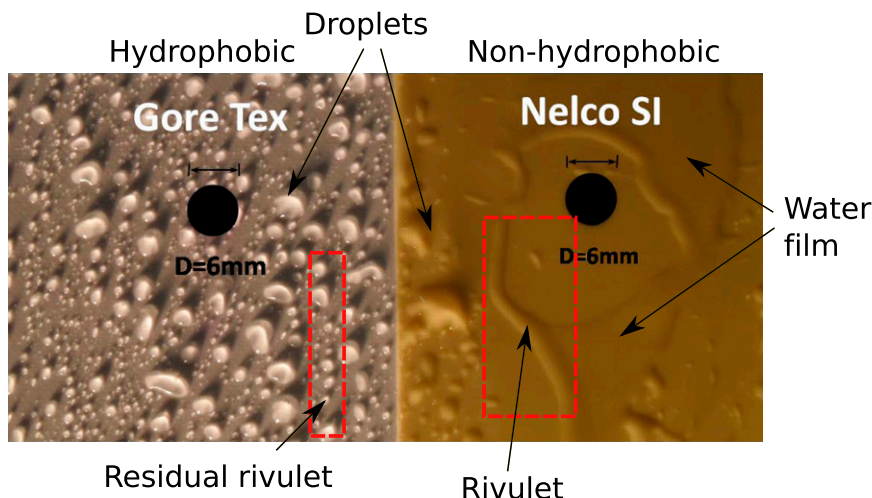
$$t_s = \sqrt[3]{\frac{3\mu Ga}{2\rho g}}, \tag{1}$$

FIG. 3. Water formation on hydrophobic and nonhydrophobic surfaces: (left) Gore-Tex fabric material and (right) fiberglass or Nelco SI.

where G represents the volumetric flow rate or rain rate $(m\,s^{-1})$ running on the radome surface; μ is the kinematic viscosity of the water $(kg\,m^{-1}\,s^{-1})$; ρ is the density of the water $(kg\,m^{-3})$; g is the gravitational acceleration $(m\,s^{-2})$; and a is the radius of the radome sphere (m). For a flat inclined surface, the model is expressed using Eq. (2) (Coulson et al. 1999). The width of the surface is represented by W (m), and θ represents the angle of inclination of the radome surface:

$$t_f = \sqrt[3]{\frac{3\mu G}{W\rho g \sin(\theta)}}. \qquad (2)$$

Figure 2a illustrates two types of radomes (spherical and flat) at 10 GHz affected by an accumulation of water over their surfaces. The spherical radome has a diameter of 2.7 m to protect a dish antenna that provides an antenna beamwidth of $2° \times 2°$. The radome protects a flat phased-array antenna (PAR) $1\,m \times 1\,m$ in area that also provides an antenna beamwidth of $2° \times 2°$. A uniform film of water has a calculated thickness based on the expression in Eq. (1) for a semispherical radome and Eq. (2) for a tilted flat radome. Knowing the thickness of the water film and the dielectric constant, one additional layer was added at the front of the dry radome model. Figure 2b shows the one-way attenuation versus rain rate for the flat radome for different tilt angles. As expected, the larger surface area of the semispherical radome tends to accumulate more water and, consequently, more attenuation is obtained with respect to the tilted plane radome.

Water formation on a radome surface can be presented in several forms—droplets, rivulets, and partial and full film. Previous observations (Fenn 1997) of wet radome surfaces show that the presence of water film formation and permanent rivulets only occur in the case of heavy rainfall and when the surface radome skin does not present repellent properties. Figure 3 shows a picture of two radome surfaces samples tilted 10° under rain conditions. The picture was taken after 3 h of rain accumulation, where the rain rate fluctuated from 5 to 35 mm h^{-1}. The left side shows the case of a hydrophobic surface (Gore-Tex). In this case, the water formation corresponds to a droplet distribution where the droplets' diameter varies from 0.1 to 5 mm. On the right, a standard nonhydrophobic material (Nelco SI) shows the combination of flat droplets, partial film water formation, and rivulets.

Significant progress has been made in the development of hydrophobic surfaces that improve the water contact angle (Clough 2009). Today, there are many types of hydrophobic surfaces available in different presentations: paints, fabrics, and laminates. Figure 4 shows pictures of water drops on six radome materials characterized as nonhydrophobic, hydrophobic, and superhydrophobic surfaces.

Several experimental approaches show that Gibble's formulation overestimates the amount of attenuation, since film water formation can occur at a high precipitation level and in cases of nonrepellent surfaces. Table 1 presents some comparative results based on theoretical and experimental data. In all cases, and especially in the higher frequencies (5, 10, and 20 GHz), a significant reduction in two-way attenuation is obtained.

Most designs of antenna radomes for weather applications include a water-repellent surface (hydrophobic and superhydrophobic) to prevent water film formation
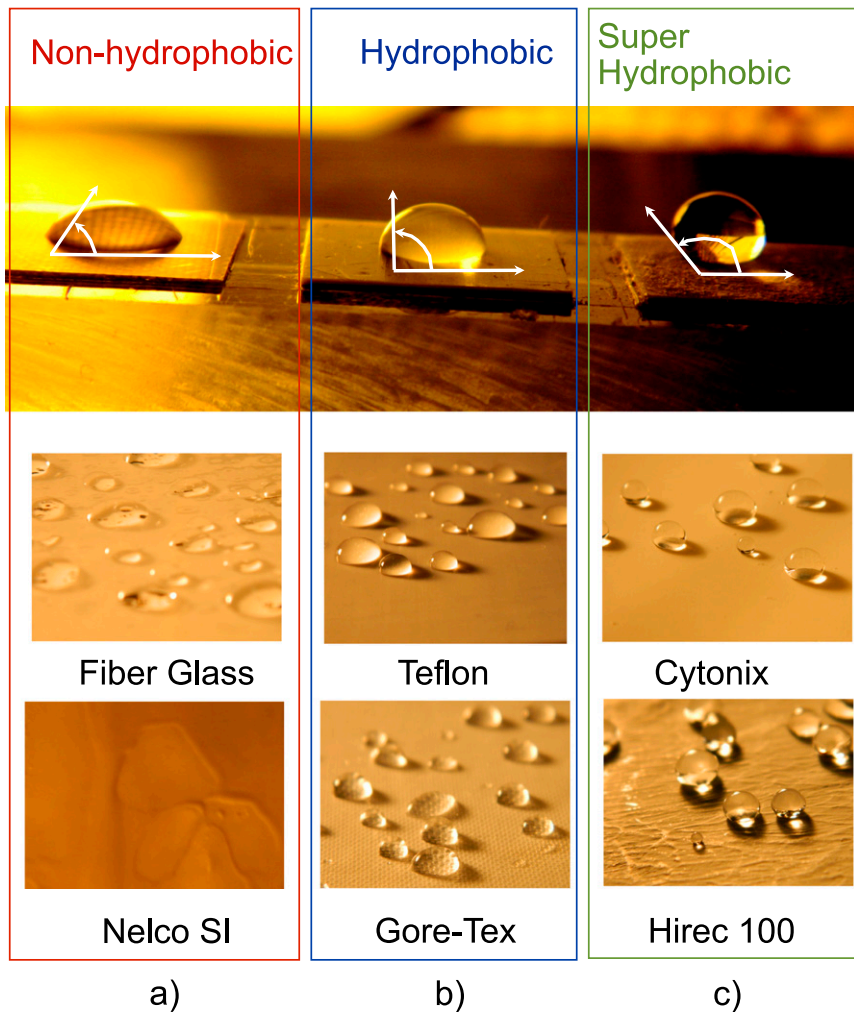
FIG. 4. Water formation on radome surfaces: (a) nonhydrophobic, (b) hydrophobic, and (c) superhydrophobic surfaces.

or rivulets. This is an effective and inexpensive solution to reduce attenuation, reflections, and depolarization of the radar signals. However, there are concerns with such water-repellent surfaces regarding their lifetime and their performance degradation over time when exposed to temperature, humidity, ultraviolet rays, air pollution, and dust. Weigand (1973) evaluated the contact angle of several radome hydrophobic samples used for airport surveillance radar. That study shows that weather and pollution reduce the contact angle up to 30° in an interval of time between 3 and 9 months.

In 2009, the Support Center for Advanced Telecommunications Technology Research (SCAT 2009) reported the results of an investigation that focused on reducing the attenuation in the radome for 9 GHz. Experimental results in a semispherical radome cover with a superhydrophobic coating (HIREC 100), supplied by Nippon

Telegraph and Telephone-Advanced Technology (NTT-AT), shows a significant reduction in one-way attenuation for heavy rainfall. The improvement factor in one-way attenuation when the rainfall rate varies between 40 and 300 mm h^{-1} is between 9 and 14. Several studies (Kurri and Huuskonen 2008; SCAT 2009) have reported that those materials are very sensitive to pollution, dirt, sand, rain, and ice erosion. Significant degradation of the water contact angle has been observed in a short period of 4–6 months; after that, the radome surface requires maintenance or replacement. The SCAT report shows that the lifetime of the superhydrophobic coatings is relatively short (less than 6 months). Samples were irradiated by ultraviolet rays in an accelerated weathering system and also exposed to a real environment; they showed significant degradation in the contact angle from 156° to 120° in 6 months.

3. Proposed wet radome model

The model proposed consists of estimating the attenuation, reflection, and depolarization of the radar signals that pass through to a wet radome as a function of the radome shape, frequency, incident angle, radome skin material, and rain conditions. The input parameters are raindrop size distribution, frequency of operation, radome geometry, radome multilayer lamination, and materials. The model is subdivided into four parts, or submodels. The first part consists of projecting the rain on a flat tilted surface called a unit cell and estimating the drop size distribution on the unit cell surface. The second part introduces the characteristics of the skin radome surface and reestimates the drop size distribution as a function of the tilted angle and hydrophobic characteristics of the radome surface. The third section estimates the equivalent effective dielectric constant of a volume that confines the droplets and air. The fourth and last submodel includes the wet layer in a multilayer radome structure and estimates the attenuation, reflection, and depolarization as a function of the incident angle (in elevation and azimuth), rainfall rate, and frequency. The concept of the wet radome model is represented in Fig. 5.

a. Surface drop size distribution (S-DSD) model for flat tilted unit cell

The first section estimates the DSD of a rain event. In this approach, the rain DSD is assumed to follow a modified gamma distribution adopted from Zhang et al. (2001):

$$n(D) = N_o D^u \exp(-\Lambda D) \quad (0 < D < D_{\max}), \quad (3)$$

$$\Lambda = 4.2 R^{-0.21} \quad (\mathrm{mm}^{-1}), \quad (4)$$

$$N_o = 8 x 10^3 \quad (\mathrm{m}^{-3} \, \mathrm{mm}^{-1}), \quad (5)$$

$$u = -0.016 \Lambda^2 + 1.213 \Lambda - 1.957, \quad (6)$$

where D represents the drop diameter, and u, Λ, and N_o are the model fit parameters defined in Zhang et al. (2001) and Doviak and Zrnić (1993).

b. Drop removal model versus tilt angle

The second part of the model estimates the distribution of liquid water droplet sizes $n_R(D)$ over the flat tilted radome surface area (A_u):

$$n_R(D) = \frac{n(D)}{v(D) A_u \cos(\theta_t) T \Delta D} \times 10^6 \quad (0 < D < D_{s-\max}), \quad (7)$$
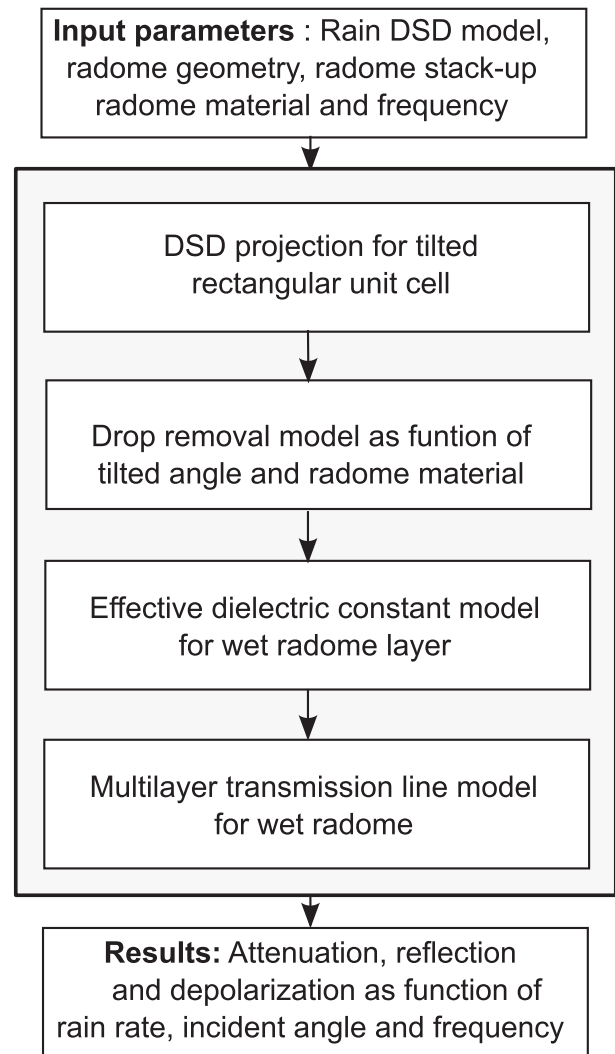
FIG. 5. Representation of a proposed wet radome model.

where $v(D)$ is the terminal velocity of the water droplet in air, ΔD is the bin width of each drop size class, T represent the integration time, and θ_t is the inclination angle of the radome surface (Lam et al. 2011).

To achieve the DSD modeled in Eq. (7), a random number generator is used to create a distribution of droplets. To estimate the DSD in a tilted radome surface using Eq. (7), properties of the radome skin, such as surface tension and contact angle hysteresis, are required to include the dynamic and drops and rivulet formation. A mathematical expression that helps in understanding the origin of the rivulets and also permits a better characterization of the DSD for an inclined surface is detailed in Eq. (8), as found in Nilsson and Rothstein (2012). This expression represents the critical angle, which is the angle where the gravity force defeats the surface tension of the droplet on a given tilted surface. In the proposed model,
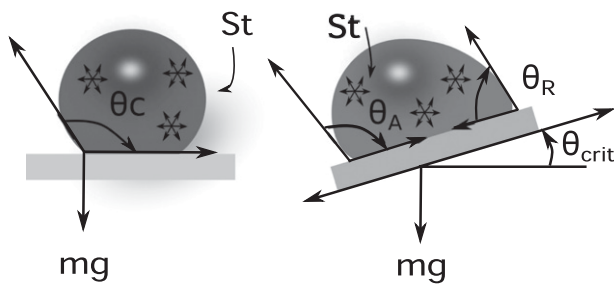
The figure flowchart reads:

Input parameters : Rain DSD model, radome geometry, radome stack-up radome material and frequency

↓

DSD projection for tilted rectangular unit cell

↓

Drop removal model as funtion of tilted angle and radome material

↓

Effective dielectric constant model for wet radome layer

↓

Multilayer transmission line model for wet radome

↓

Results: Attenuation, reflection and depolarization as function of rain rate, incident angle and frequency

FIG. 6. Representation of contact, advancing, and receding angles in a horizontal and tilted surface. The water surface tension is represented by St.

Eq. (8) is used to remove the droplets that start when the gravity forces defeat the surface tension. The critical angle depends of the diameter of the water, properties of the water, and surface characteristic of the skin radome (hysteresis, advancing, and receding angles). In case of hydrophobic and superhydrophobic materials, under rain conditions, only the radome surfaces droplets are observed. When the drop diameter is big enough, the gravity force defeats the surface tension. The droplet will run; if there are more droplets in its way, they might collide and then break in small droplets. In the case of non-hydrophobic materials, when the gravity force defeats the surface tension, the drop starts running; a large part of it runs as a drop, the rest remains as a thin rivulet. On a hydrophobic material, rivulet formation does not occur at a given location. The origin of each rivulet happens when the gravitational force defeats the surface tension of a droplet on the radome surface. The inclination angle and the number and size of droplets define the number of rivulets on a given surface. In the model proposed, the dynamics of the rivulets was not included. The model can estimate the number of rivulets and can also estimate how long this rivulet can be.

Figure 6 illustrates the surface water surface tension and gravity force for a drop in horizontal and tilted positions as a function of the contact, and advancing and receding angles,

$$\alpha_{\mathrm{crit}} = \sin^{-1}\left[\frac{6k^{-2}\sin\left(\pi - \frac{1}{2}\sin\theta_H\right)(\cos\theta_H - \cos\theta_A)}{D^2}\right],$$
(8)

where θ_R is the receding angle and θ_A is the advancing angle. The hysteresis angle is then represented by $\theta_H = \theta_R - \theta_A$ and k^{-1} is the capillarity length, which is 2.7 mm for water. Figure 7a illustrates the critical angle versus drop size diameter for different hydrophobic (Teflon and Gore-Tex) and superhydrophobic

(Teflon S240, HIREC 100, and Cytonix WX2100) material surfaces.

The water contact angle (θ_C) is a common parameter used to characterize the surface materials' hydrophobic properties in static conditions. However, for better characterization of the hydrophobic materials in dynamic conditions, the advancing (θ_A) and receding (θ_R) contact angles are the parameters required. To estimate the advancing and receding angles, the drop expansion and contraction process or dynamic tensile drop method is used. This method determines the largest contact angle possible without increasing its solid/liquid interfacial area by adding volume dynamically. This maximum angle is the advancing angle. Volume is removed to produce the smallest possible angle, the receding angle. The difference between the advancing and receding angle is the hysteresis contact angle (θ_H) (Nilsson and Rothstein 2012). Surfaces that present a lower hysteresis angle are better hydrophobic materials. Any small perturbation can easily remove the droplets from the surface. A higher water contact angle than 120° and a lower hysteresis angle than 10° results in a new category of better hydrophobic surfaces called superhydrophobic materials, which promise a lower accumulation of water on the radome surface (Sas et al. 2012). Figure 7 illustrates the advancing, receding, and hysteresis angles of six samples obtained in the Fluid Dynamic Laboratory at University of Massachusetts Amherst, based on the drop expansion and contraction process. Details of the advanced (θ_A), receding (θ_R), and hysteresis angles (θ_H) are presented in Table 2.

c. Effective dielectric constant (EDC) model for wet radome unit cell

Once the drop spectra on the radome surface have been calculated, the next step is to estimate the effective dielectric constant of the wet surface. In the case of the drop formation, we consider a volume composed of semispherical droplets and air. The area of the unit cell represents the volume, and the height of the unit cell can be estimated as a function of the largest drop diameter. Considering that the droplets are small compared to the wavelength (in the case of S, C, and X bands), the Maxwell–Garnet mixing formulation can be used (Sihvola 2000). Equation (9) estimates the effective dielectric constant based on a fraction volume (f) of the droplets and air in the specified volume, as illustrated in Fig. 8:

$$\varepsilon_{\mathrm{eff}} = \varepsilon_2 + \frac{3f\varepsilon_2(\varepsilon_1 - \varepsilon_2)}{\varepsilon_1 + 2\varepsilon_2 - f(\varepsilon_1 - \varepsilon_2)},$$
(9)

where f is the fractional volume of formed water droplets with dielectric constant (ε_1) over the radome surface
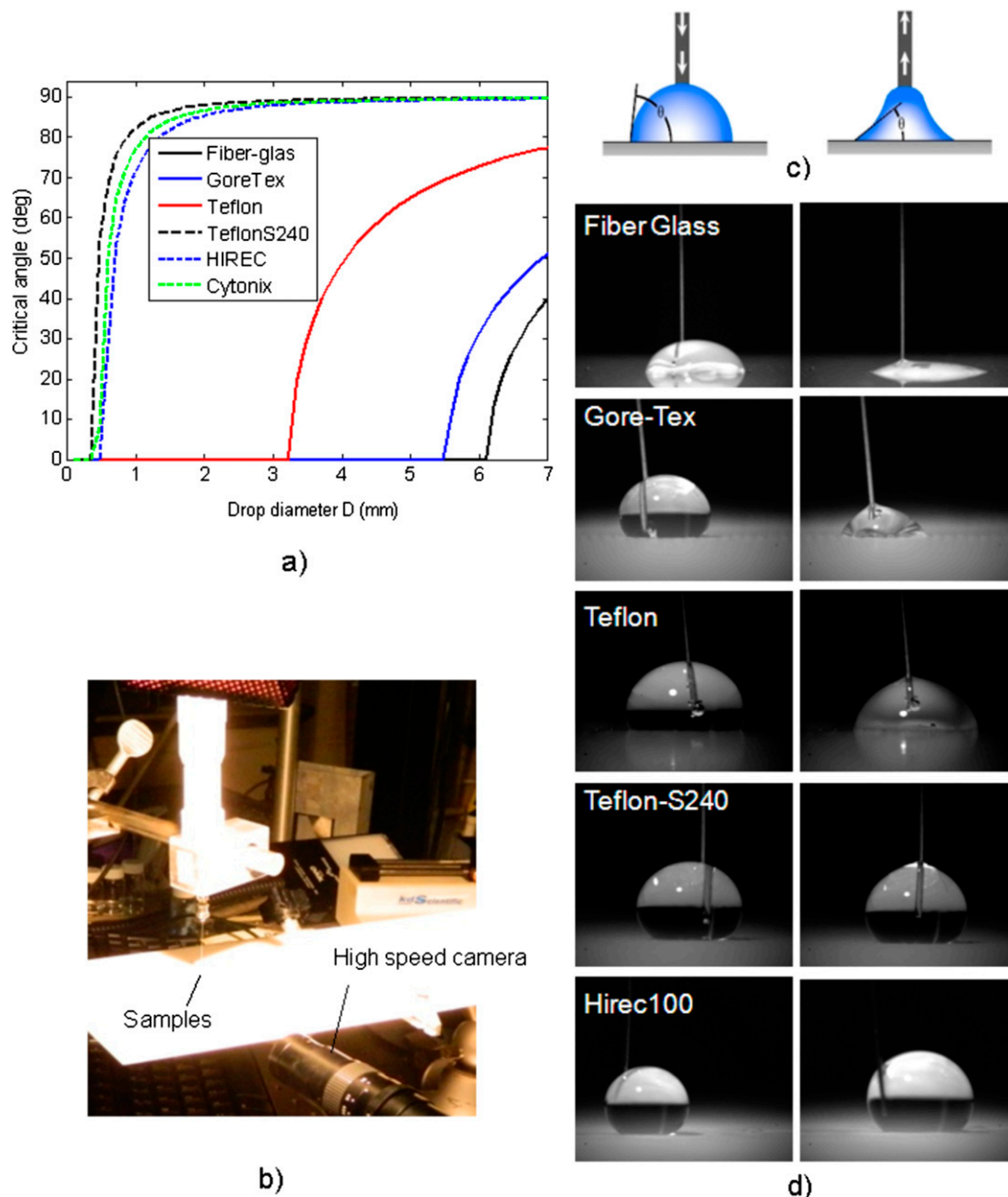
FIG. 7. (a) Critical angle vs drop diameter for nonhydrophobic (fiberglass), hydrophobic (Gore-Tex and Teflon) and superhydrophobic (HIREC, Teflon S240, and Cytonix). (b) Experimental setup for drop expansion and contraction process. (c) Method to characterize the (left) advancing and (right) receding contact angles for (d) nonhydrophobic (fiberglass), hydrophobic (Gore-Tex, Teflon) and superhydrophobic (Teflon-S240B and HIREC 100) materials.

and the dielectric constant of the air (ε_2). The volume is defined based on the unit cell area and the maximum droplet diameter estimated in the previous section.

d. Multilayer stack-up wet radome model

The fourth and last part of the model consists of estimating the scattering parameters of the radome for any angle of incidence (in the azimuth plane) and polarization mode (vertical and horizontal). This model was formulated using the equivalent transmission line method. To describe the behaviors of the electric fields in a dry radome structure, a well-known mathematical model based on the equivalent transmission line method is used (Hirsch and Grove 1988). This basic model was expanded for a multilayer medium and also to include the effect of water formation.

TABLE 2. Advancing (θ_A), receding (θ_R), and hysteresis (θ_H) angles for nonhydrophobic, hydrophobic, and superhydrophobic materials used for the outer skin of the radome layer.

Material	Category	θ_A (°)	θ_R (°)	θ_H (°)
Fiber glass	None	105	15	82
Gore-Tex	Hydrophobic	120	47	73
Teflon	Hydrophobic	120	79	41
Teflon S240	Superhydrophobic	150	144	6
HIREC 100	Superhydrophobic	151	144	7
Cytonix WX2100	Superhydrophobic	160	151	9

We consider a multilayer medium with a boundary at $x = t_1, t_2, t_3$, as shown in Fig. 9. Each sandwich radome layer is composed of a homogeneous material with dielectric and magnetic constants (ε_n, μ_n). Reflected energy was modeled as a series of reflections, as represented in Fig. 9b, with a portion of the incident wave energy transmitted into the medium 2 ($x = -t_1$), at which point some of the energy reflects back from the medium 3 ($x = -t_2$) and so on. Assuming an incident plane wave in medium 1, the formulation for the transmission and reflection coefficients for a parallel (horizontal) and orthogonal (vertical) polarization can be represented in Eqs. (10)–(16).

In the multilayer radome model, represented in Fig. 9, the incident angle is represented by θ_i and transmitted and reflected angles by θ_t and θ_r, respectively. The transmitted signal in a multilayer radome (n layers) can be estimated using Eq. (10). The impedance characteristic [$\eta_{t(n)}$] of each layer can be estimated using Eq. (11). In this expression t_n represents the thickness of each radome layer. The reflections (Γ_H and Γ_V) and transmission coefficients (T_H and T_V) for H and V polarization in each layer can be obtained by the expressions (14) and (15):

$$\theta_{t(n+1)} = \cos^{-1}\left(\sqrt{1 - \frac{\varepsilon_{rt(n)}}{\varepsilon_{rt(n+1)}} \sin(\theta i_{t(n)})^2} \right) \qquad (10)$$

$$\eta_{t(n)} = \eta_{t(n+1)} \left[\frac{\eta_{t(n)} + j\eta_{t(n+1)} \tan(\beta_{t(n+1)}t_n)}{\eta_{t(n+1)} + j\eta_{t(n)} \tan(\beta_{t(n+1)}t_n)} \right] \qquad (11)$$

$$\Gamma_{Ht(n)} = \frac{\eta_{t(n+1)} \cos\theta t_{t(n+1)} - \eta_{t(n)} \cos\theta i_{t(n)}}{\eta_{t(n+1)} \cos\theta t_{t(n+1)} + \eta_{t(n)} \cos\theta i_{t(n)}} \qquad (12)$$

$$\Gamma_{V(t_n)} = \frac{\eta_{t(n+1)} \cos\theta i_{t(n)} - \eta_{t(n)} \cos\theta t_{t(n+1)}}{\eta_{t(n+1)} \cos\theta i_{t(n)} + \eta_{t(n)} \cos\theta t_{t(n+1)}} \qquad (13)$$

$$T_{Vt(n)} = \frac{2\eta_{t(n+1)} \cos\theta i_{t(n)}}{\eta_{t(n+1)} \cos\theta i_{t(n)} + \eta_{t(n)} \cos\theta t_{t(n+1)}} \qquad (14)$$
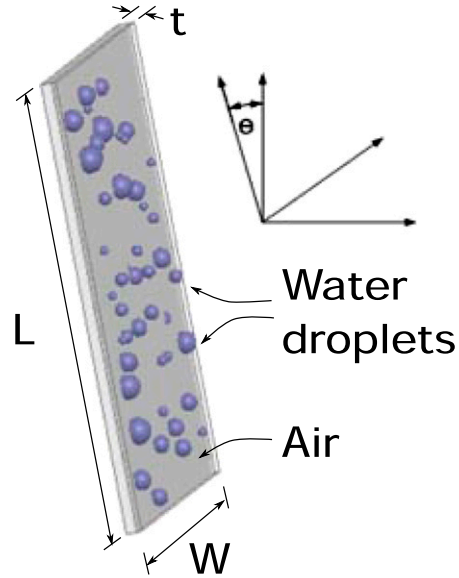

FIG. 8. Representation of wet radome unit cell composed of air and water droplets.

$$T_{Ht(n)} = \frac{2\eta_{t(n+1)} \cos\theta i_{t(n)}}{\eta_{t(n+1)} \cos\theta t_{t(n+1)} + \eta_{t(n)} \cos\theta i_{t(n)}} \qquad (15)$$

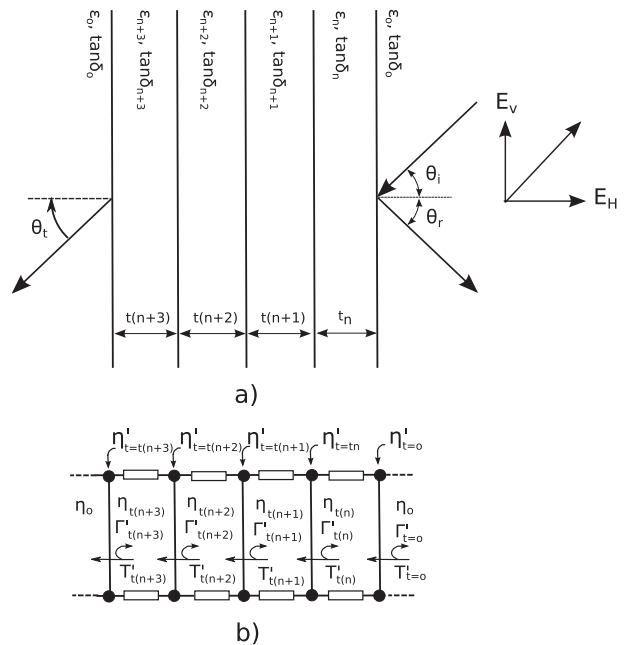The cross polarization introduced by the radome can influence the performance of the radar system and can

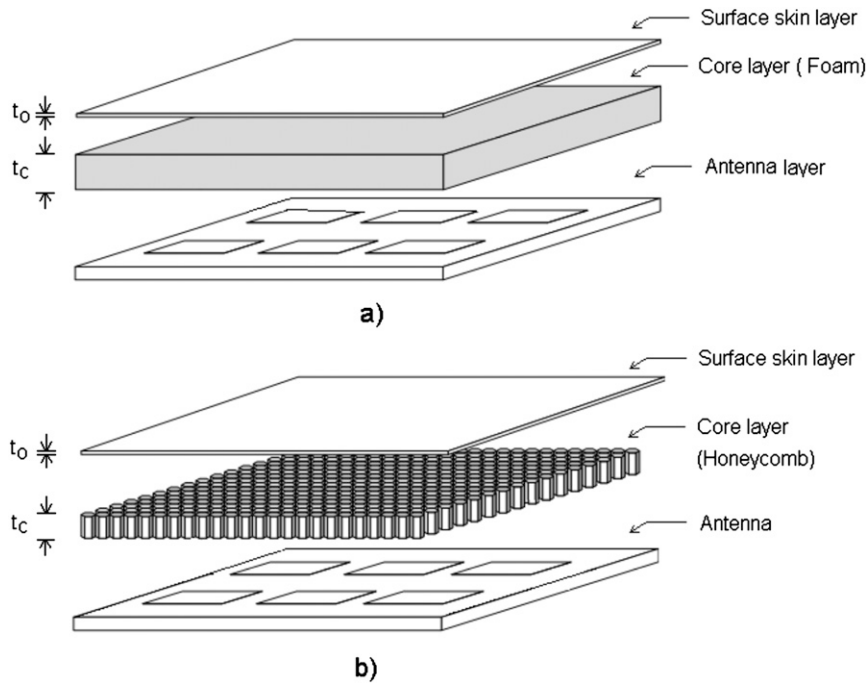FIG. 9. Radome model representation: (a) multilayer radome and (b) circuital transmission line model.

FIG. 10. (a) Foam sandwich wall structure radome using Gore-Tex as a skin layer and Rohacell 31HF foam as a dielectric core (t_o = 12 mil, t_c = 250 mil). (b) Honeycomb sandwich wall structure radome, using Gore-Tex as a skin material and Rohacell 31HF as a dielectric core (t_o = 12 mil, t_c = 250 mil).

be critical for a polarimetric radar system that requires extreme isolation between polarization channels. To evaluate cross polarization induced by a radome, we use the results of Rudge et al. (1982),

$$D_{t(n)} = \sqrt{\frac{1 - 2K_{t(n)}\cos[\phi_{Ht(n)} - \phi_{Vt(n)}] + K_{t(n)}^2}{\cot^2\theta i_{t(n)} + 2K_{t(n)}\cos[\phi_{Ht(n)} - \phi_{Vt(n)}] + K_{t(n)}^2 \tan^2\theta i_{t(n)}}}$$ (16)

where D represents the depolarization ratio, K represents the ratio of the transmission coefficients $K = T_H/T_V$, and ϕ_H and ϕ_V represent the respective phases. In order to illustrate the use of the previous formulation, two sandwich flat radomes, as depicted in Fig. 10, are used as examples. The first one is composed of a thin hydrophobic skin layer (Gore-Tex) and a thick foam (Rohacell) layer. The second is also a sandwich radome, composed in the same manner, using a Gore-Tex hydrophobic skin layer and a thick honeycomb layer. For both radomes, the calculated transmission coefficient is lower than −0.4 dB and the reflection coefficient is lower than −25 dB for an incident angle that varies from 0° to 60° in the azimuth plane (see Fig. 11). The cross polarization induced by these two radomes is very small. A maximum distortion of −34 dB can occur in the incident angle range from 0° to 60°. Small differences between both radomes are due to the dielectric constant in the honeycomb being slightly higher than that

for the Rohacell. Electrical and mechanical properties of radomes used as examples are presented in Table 3.

4. Results and validation

Three samples of nonhydrophobic (fiberglass) and hydrophobic (Gore-Tex) materials were exposed to moderate rain on 21–24 September 2011. Each set had a surface area of 9 cm × 9 cm and was tilted −10°, 0°, and +10°, respectively, and then left for an interval of 4.5 h, where rain fluctuated from 0.1 to 45 mm h^{-1}. Photographs with a digital high-resolution camera were taken at intervals of 30 min. The average reflectivity data were obtained from two nearby S-band radars in Boston, Massachusetts, and Albany, New York. Figure 12a illustrates the average radar reflectivity and the rainfall rate estimated using the expression Z–R, defined in the following equation:
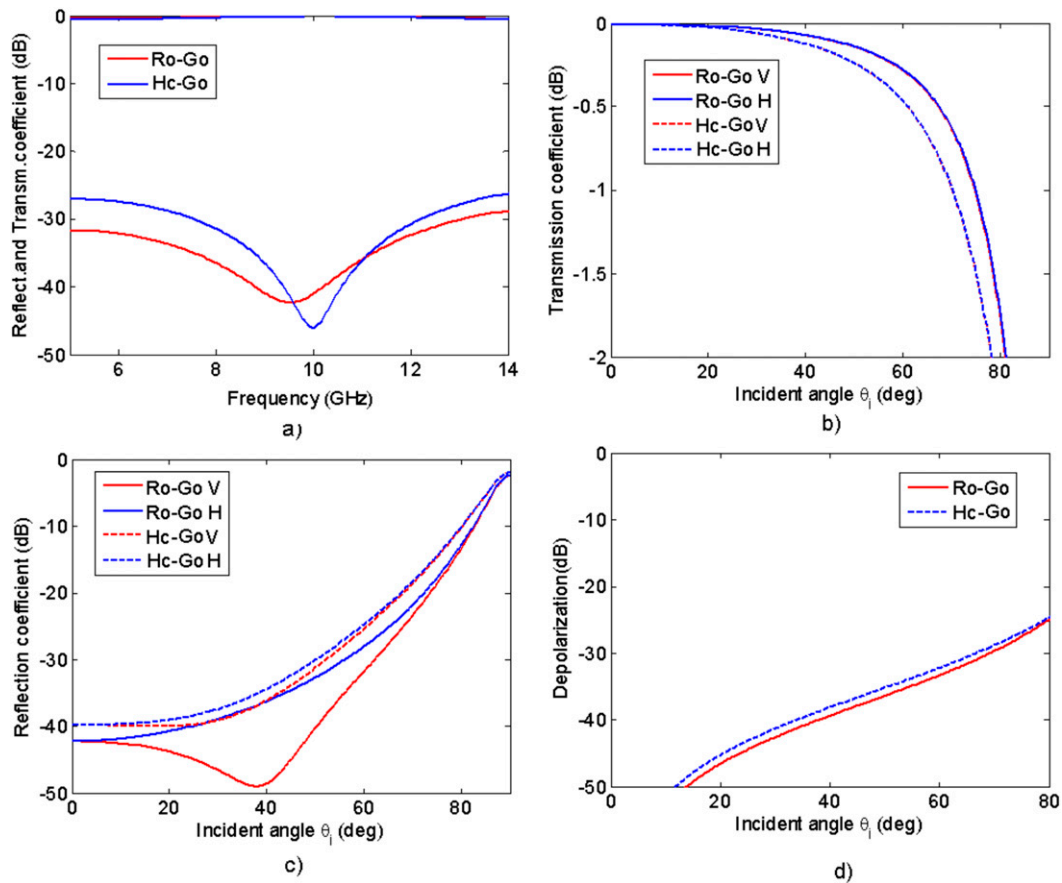
$$Z = 250R^{1.2},$$ (17)

FIG. 11. Calculated results of dry sandwich radomes using Gore-Tex/foam (Ro-Go), and Gore-Tex/honeycomb (Hc-Go). (a) Transmission and reflection coefficients vs frequency. (b) Reflection coefficients vs incident angle (azimuth plane) for H and V. (c) Transmission coefficients vs incident angle (azimuth plane) for H and V. (d) Depolarization ratio vs incident angle (azimuth plane).

where Z is the reflectivity in non-logarithmic units and R is the rain rate in millimeters per hour. Figures 12c,d show pictures of the water accumulated on three Gore-Tex radome samples tilted at $-10°$, $0°$, and $+10°$ and exposed for 2 h and 51 min under the same rain event (on 23 September 2011). The droplets were counted and measured manually, and then represented in the histogram plots for each tilt angle (after 2 h and 51 min). As expected, the samples at large tilted angles show more droplets accumulated.

Using the rain rate estimated from the reflectivity of S-band [Next Generation Weather Radar (NEXRAD)]

radar using the Z–R relationship given in (17) (Doviak and Zrnić 1993) and the radome hydrophobicity properties (hysteresis angle), an initial DSD in the radome surface was estimated using Eq. (7). To exclude the droplet that runs in the surface, when the gravity force defeats the surface tension, Eq. (8) is used. This expression estimates the maximum diameter of the droplet that can be held in the radome surface, and then droplets with larger diameters are removed from the original drop size distribution to give more accurate representation of the DSD in the radome surface.

TABLE 3. Properties for radome materials.

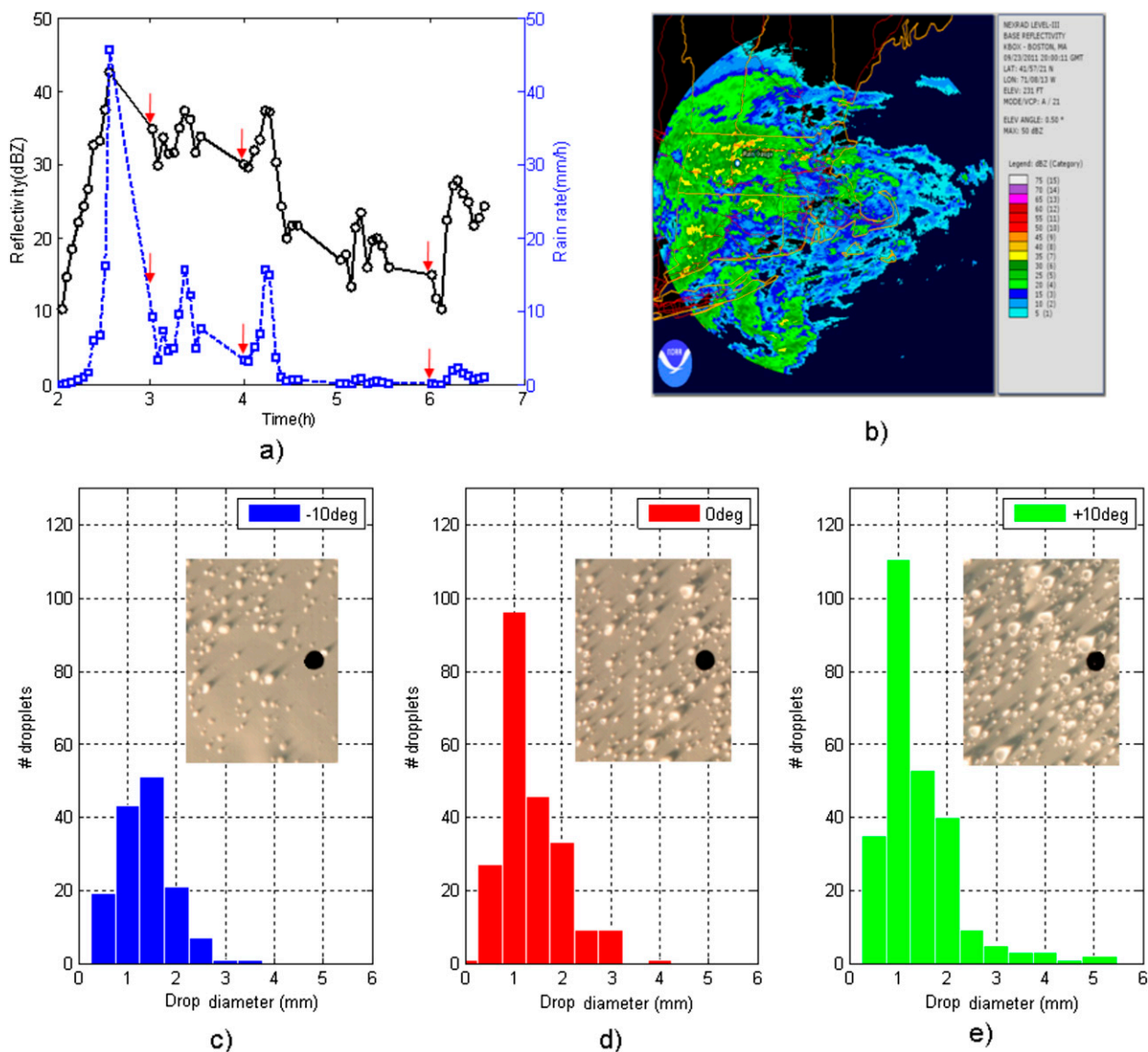| Material	Density ($g\,cm^{-3}$)	Dielectric constant (10 GHz)	Tangent loss (10 GHz)	Thermal conductivity ($W\,m\,K^{-1}$)	Water absorption 98HR (%)
Rohacell 31HF	0.0031	1.046	0.0017	0.029	23
Honeycomb HR11/83	0.0048	1.06–1.09	—	0.064	4.4
Gore-Tex RA7906	0.2–2.0	1.55	0.0005	0.1–0.3	0.0
Rogers 5880 LZ	1.37	1.96	0.0027	0.2–0.22	0.22
Nelco SI	1.79	3.2	0.0080	0.294	0.10

FIG. 12. DSD on radome surface based on rainfall rate DSD. (a) Reflectivity and rain rate obtained from rain experiment 4 (23 Sep 2011). (b) Reflectivity data from NEXRAD radar at Boston. (c) Picture and DSD of water droplets accumulated on a Gore-Tex surface tilted −10°. (d) Picture and DSD of sample of water droplets accumulated on a Gore-Tex surface tilted 0°. (e) Picture and DSD of water droplets accumulated on a Gore-Tex surface tilted +10°.

Figure 13 illustrates the comparison results of the drop size distribution on the Gore-Tex sample tilted at +10°. Although the estimated and measured distributions do not match perfectly, the median values of the drop diameter differ only by 0.01 mm. More cases and experimental results that include dual-polarized data are needed to provide statistical validation of the proposed model.

Measured wet radome radar data

We used the case in which radar data from X- and S-band radars were employed to estimate the radome attenuation of the Integrated Project 1 (IP1) CASA X-band radars under rain conditions (Trabal et al. 2008). Reflectivity data of a precipitation event (20 June 2007) were observed by CASA IP1 radar (Junyent et al. 2010) and the WSR-88D (KTLX; Oklahoma City, Oklahoma). The convective line event seen by S-band KTLX radar coming from the northwest passed through the CASA radar network area (Fig. 14). Data were collected by the four CASA X-band radars and the KTLX S-band radar. The storm extended more than 140 km in length and 40 km in width, resulting in severe attenuation on three [Cyril, Oklahoma (KCYR); Rush Springs, Oklahoma
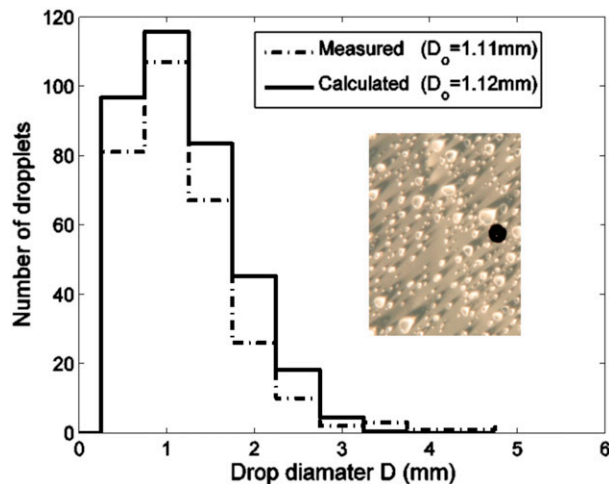
FIG. 13. Comparison of estimated and measured DSD collected on a hydrophobic (Gore-Tex) radome sample (5 cm × 5 cm). The measured data correspond with data obtained in experiment 4 on 23 Sep 2011.

(KRSP); and Chickasha, Oklahoma (KSAO)] of the four radars simultaneously.

Figure 15 shows a comparison of the reflectivity between the CASA KRSP X-band and the KTLX S-band radars averaged over an area of 750 km^2. A short period of severe radome attenuation is clearly identified during the half hour ranging from 6 to 6.5 UTC (decimal time), with a maximum observed attenuation of 7.5 dB. The reflectivity estimated over the X-band radar wet radome by the S-band radar is also shown.

The radome of the IP1 radar system is a hemisphere-on-cylinder radome design with a diameter of 2.7 m designed to operate from 9 to 10 GHz. The wall construction (A-sandwich radome) consists of two epoxy/fiberglass skin layers and a honeycomb core as an inner layer. A thin layer of CRC 6000 hydrophobic coating (with a contact angle of 140°) was applied to prevent the formation of film water. In the case of WSR-88D, the radome is a rigid, truncated spherical with a diameter of 11.9 m; each radome panel is made individually as a geodesic fiberglass panel with a layered foamlike substance that has a Tedlar overlay. On top of the Tedlar overlay, the surface has up to a 3-mm-thick coat of Amron that provides repellent characteristics. The radome was designed to perform with transmission losses below 0.125 dB. According to the specifications for the WSR-88D, the radome is maintained every 8 months and inspected every year.

Figure 16 shows the corresponding calculated and measured values of the two-way attenuation radar signals for a reflectivity range from 0 to 50 dBZ. The scatter data were obtained by comparing the difference between the S- and X-band wet radomes. The area was averaged over a rain gauge network with a size of 20 km × 32 km. The calculated data (dashed line) was estimated using the radome characteristics and geometry for a rain intensity equivalent to a reflectivity from 0 to 50 dBZ in intervals of 5 min. A good fit existed between measured and calculated values, which suggests that the proposed model can be used to estimate the two-way losses of a wet radome surface for this case. Figure 16 shows the scattered radar data represents the two-way attenuation of the IP1 radar. The blue dashed line is the fitted curve that represents the scattered IP1 radar data. About 0.13 dB is the root-mean-square (RMS-1) value between the data
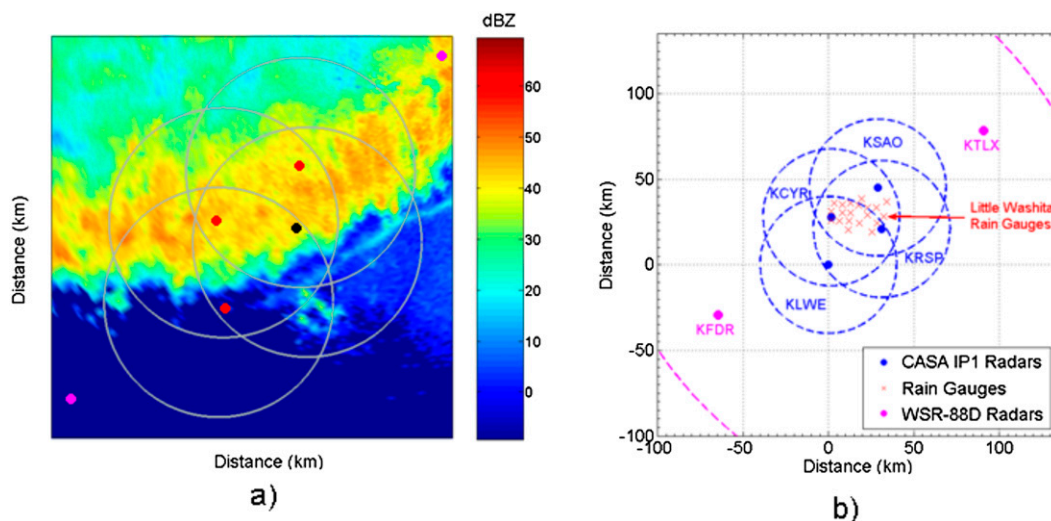

FIG. 14. Validation results of wet radome model for IP1 X-band radome. (a) Storm event (20 Jun 2007) in Oklahoma. (b) Representation of relative locations of IP1 radar network nodes, NEXRAD radars, and rain gauge network in Oklahoma.
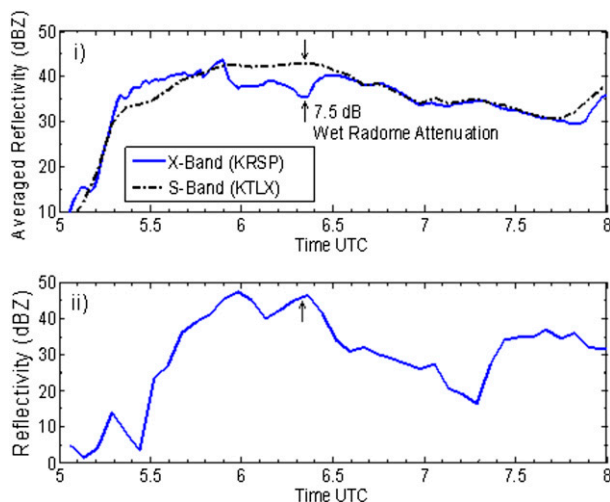
FIG. 15. Averaged reflectivity for the X- and S-band radars during the storm event (i) and S-band reflectivity over the X-band wet radome during the same time and day (ii). The reflectivity over the X-band radar wet radome by the S-band radar.
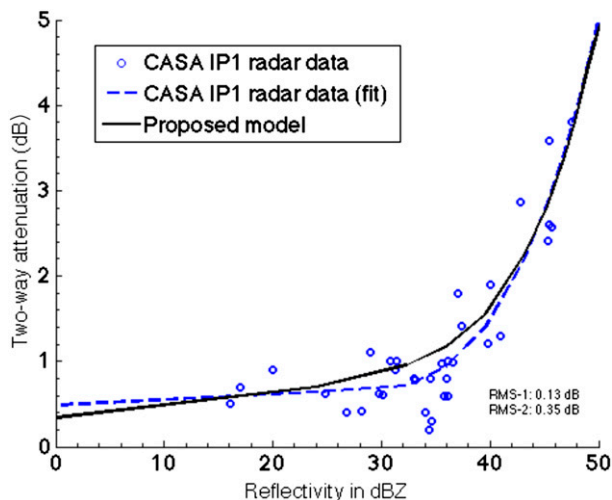

FIG. 16. Validation results of wet radome model for IP1 X-band radome. Calculated and measured values of the two-way attenuation radar signals for reflectivity range between 0 and 50 dBZ. Scattered radar data represent the two-way attenuation of the IP1 radar. The blue dashed line is the fitted curve that represents the scattered IP1 radar data. About 0.13 dB is the RMS-1 value between the data obtained using the proposed model and fitted curve radar data. And about 0.35 dB is the RMS-2 value between the scattered radar data and the fitted curve that represents the measured radar data.

obtained using the proposed model and the fitted curve radar data. And about 0.35 dB is the root-mean-square (RMS-2) value between the scattered radar data and the fitted curve that represent the measured radar data.

Table 4 provides information comparing radome design specification (given by the manufacturer) and calculated values based on the model proposed. It also shows a comparison with radar data measured by Trabal et al. (2008) in dry conditions, and also for 10 and 30 mm h^{-1}: Small differences existed between specified and estimated values of two-way losses using this model for dry and wet conditions. Table 4 gives summary results of two-way attenuation in an X-band IP1 antenna dish radome.

5. Case study and model experiments

In this section, four different scenarios were selected to illustrate the utility of the proposed wet radome model. For all scenarios we chose a flat tilted radome for two reasons: First, this shape can represent the unit cell of any radome shape. Second, flat panels represent the shape of phased-array weather radars where the polarimetric variables are more sensitive to perturbation in the H and V channels. Figure 17 illustrates the representation of a semispherical radome using a polygonal tilted unit cell model to explain that this model can be used for other radome geometry.

The first case represents a situation where a flat antenna radome designed without a hydrophobic surface is tilted about 34°. The second case also represents a flat antenna radome, but this time designed with hydrophobic

film, also tilted about 34°. A third case uses the same radome; however, the tilted angle is reduced from 34° to 10°. For all three cases, the flat radome considered was designed to operate at 10 GHz, and the radome corresponded to a walled structure composed of one thin layer of 0.304 mm (12 mil) of Teflon ($\varepsilon_r = 1.55$, tan$\delta = 0.0017$) and a thick layer (250 mil) of core foam Rohacell 31HF ($\varepsilon_r = 1.07$, tan$\delta = 0.0017$). We assume for these cases a water dielectric constant of $\varepsilon_r = 60.68 + 32.79i$ and tan$\delta = 0.54$, estimated for 10 GHz and at 20°C. The final case (when rivulets are present) is discussed at the end of this section.

a. Flat radome tilted 34° without hydrophobic surface

This first scenario represents the case where the radome surface has lost its hydrophobic properties. In this

TABLE 4. Summary results of two-way attenuation in X-band IP1 antenna dish radome.

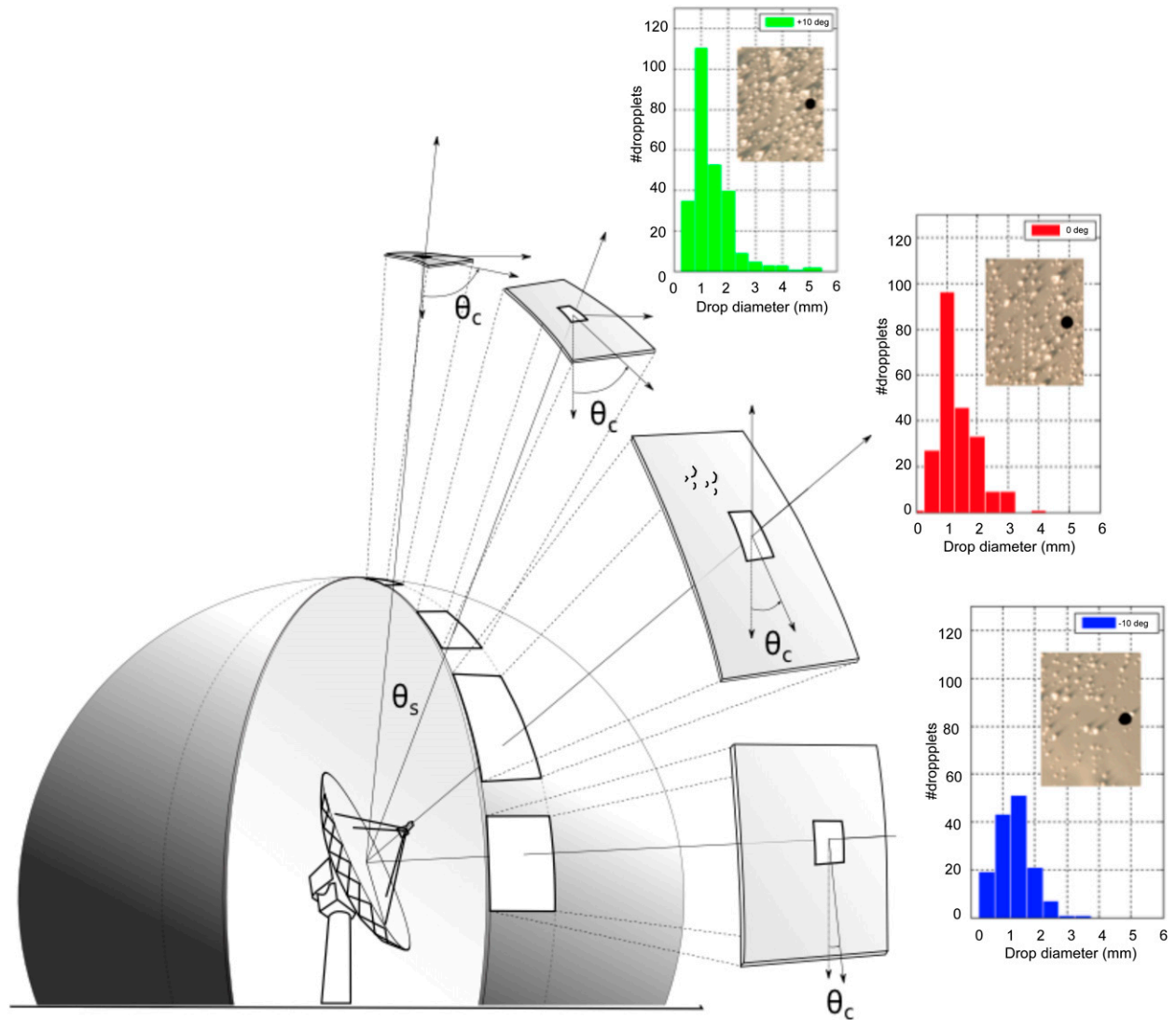| Parameter	Specified (dB)	Calculated (dB)	Measured (dB)
Two-way loss (dry)	0.8	0.50	No data
Two-way loss (at 10 mm h^{-1})	1.6	1.18	1.11
Two-way loss (at 30 mm h^{-1})	2.0	1.82	1.96

FIG. 17. Representation of possible uses of the model proposed on a semispherical radome using a polygonal tilted unit cell.

case, a formation of water film occurs and the radome performance is considered as the worst-case scenario for a radar system performance under rain condition. Figure 18 presents the transmission coefficient (one-way attenuation), reflections, and depolarization for a flat radome with a tilt angle of 34° as a function of rain rate and scan angle in the azimuth plane. Figure 18b shows one-way attenuation, which indicates that a significant attenuation (1.6–4.5 dB) can be produced for moderate and high rain intensities (10–100 mm h^{-1}). A small variation (less than 0.01 dB) between H and V is observed in the near to broadside; however, it increases up to 0.5 dB at a 45° incident angle. Figure 18c shows the reflection coefficients of the radome. Results show significant changes in reflection for H and V for a wet radome as compared to a dry radome, even for small rain intensities.

Reflections can be a concern for values higher than −10 dB, since those can considerably affect the scanning impedance of the array antenna and also the antenna patterns, principally in the sidelobe region. Figure 18d presents the cross-polarization ratio of the radome. At broadside, negligible depolarization is produced. However, when the antenna is scanned, the wet radome significantly affects the polarization of the radar signal. At 45° scanning in the azimuth plane, we observe that the radome can reduce the cross polarization by about 20 dB.

b. Flat radome tilted 34° with hydrophobic surface

In this case we replaced the skin surface with a hydrophobic material (Gore-Tex), since this material (Teflon based) is commonly used for weather radar
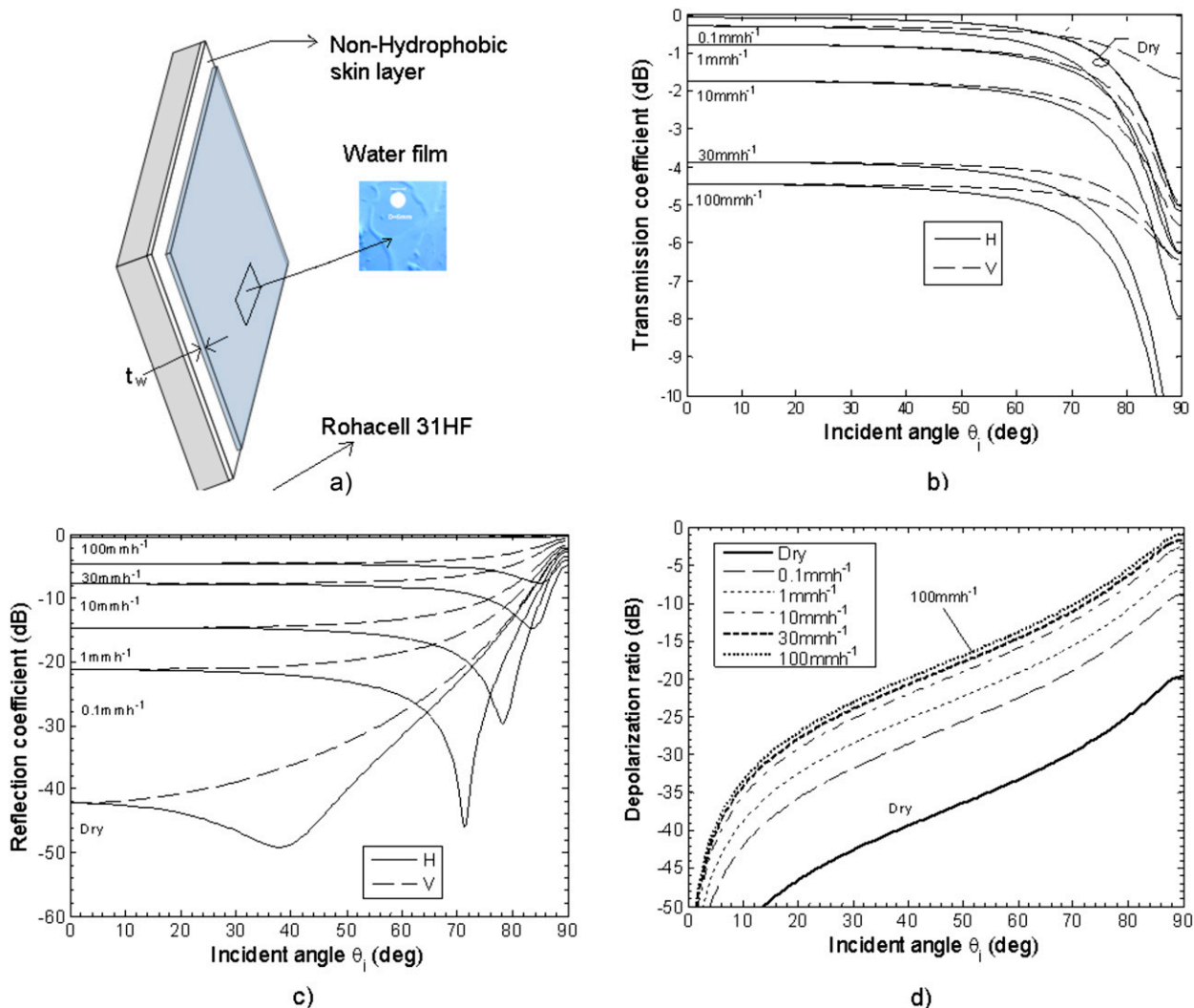
FIG. 18. Calculated results of nonhydrophobic wet radome surface tilted 34° under different rain intensities (0.1, 1, 5, 10, 30, and 100 mm^{-1}): (a) transmission coefficient vs incident angle, (b) reflection coefficient vs incident angle, and (c) depolarization ratio vs incident angle.

radomes. Figure 19 illustrates the one-way attenuation, reflections, and depolarization for a flat radome with tilt angle of 34° as a function of rain rate and scan angle in the azimuth plane. Figure 19b shows a comparison between the total attenuation of a dry radome and when the same radome is wet for different rain intensities. The results indicate that the attenuation is drastically reduced (2.9 dB below) compared to the previous case (nonhydrophobic surface) when the radome was exposed to 100 mm h^{-1}. As with the previous case, small differences in attenuation existed between H and V with respect to beam position. Figure 19c shows reflections. In the worst-case scenario, for 100 mm h^{-1}, the reflections are below −25 dB for the overall scanning range required (±45°). Figure 19d shows the cross-polarization ratio of

this radome. For ±45°, the cross polarization induced by the radome is about 14 dB (16 dB better than in the previous case).

c. Flat radome tilted 10° with hydrophobic surface

In this case we used the same radome as in the previous case, but reduced the tilt angle from 34° to 10°. Figure 20 illustrates the one-way attenuation, reflections, and depolarization for a flat radome tilted at 10° as a function of rain rate and scan angle in the azimuth plane. Figure 18b compares the transmission coefficient of a dry radome with a wet one for different rain intensities. The results indicate that a significant improvement can be obtained in the three parameters under evaluation by reducing the tilt angle of the
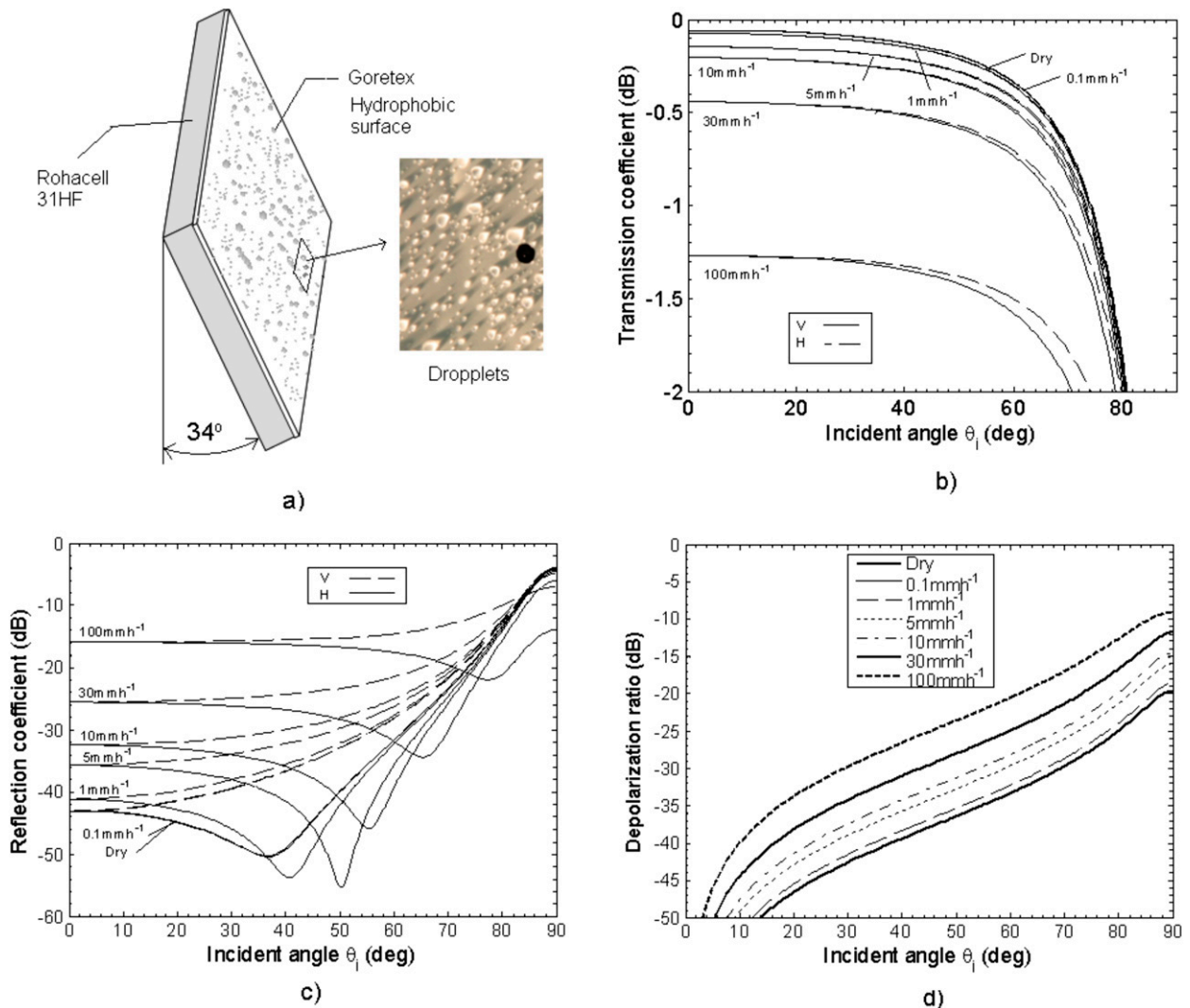
FIG. 19. Calculated results of hydrophobic (Gore-Tex) wet radome surface tilted (34°) under different rain intensities (0.1, 1, 5, 10, 30, and 100 mm h^{-1}): (a) transmission coefficient vs incident angle, (b) reflection coefficient vs incident angle, and (c) depolarization ratio vs incident angle.

antenna. For 100 mm h^{-1} at broadside, the improvement for a hydrophobic radome tilted at 34° is about 1.35 dB, and the improvement can be 4 dB for a radome without hydrophobic skin. Figure 20c shows that in the worst-case scenario, for 100 mm h^{-1} the reflections are below −35 dB for the overall scanning range required (±45°). Figure 20d shows that the cross-polarization ratio of this radome tilted 10° degrades the radar signals only 8 dB (6 dB better that the previous case, and 12 dB compared to the radome without the hydrophobic skin surface).

d. A special case when rivulets are present

Modeling rivulet formation on an inclined surface requires a sound understanding of the dynamics of droplets for a particular surface. Upon simple inspection, non-hydrophobic materials tend to spread water on a surface, creating uniform films of water that end in permanent rivulets, as illustrated in Fig. 21a. On a hydrophobic material, the location of the rivulet seems to occur randomly. A rivulet starts when gravitational forces defeat the surface tension of a droplet on the radome surface. The inclination angle, number, and size of droplets define the number of rivulets for a given surface. The mathematical expression that helps explain the origin of the rivulets and also permits the characterization of the drop size distribution for an inclined surface is detailed in Eq. (8) and can be used to estimate the number of rivulets. However, it is quite difficult to introduce rivulets in the proposed model.
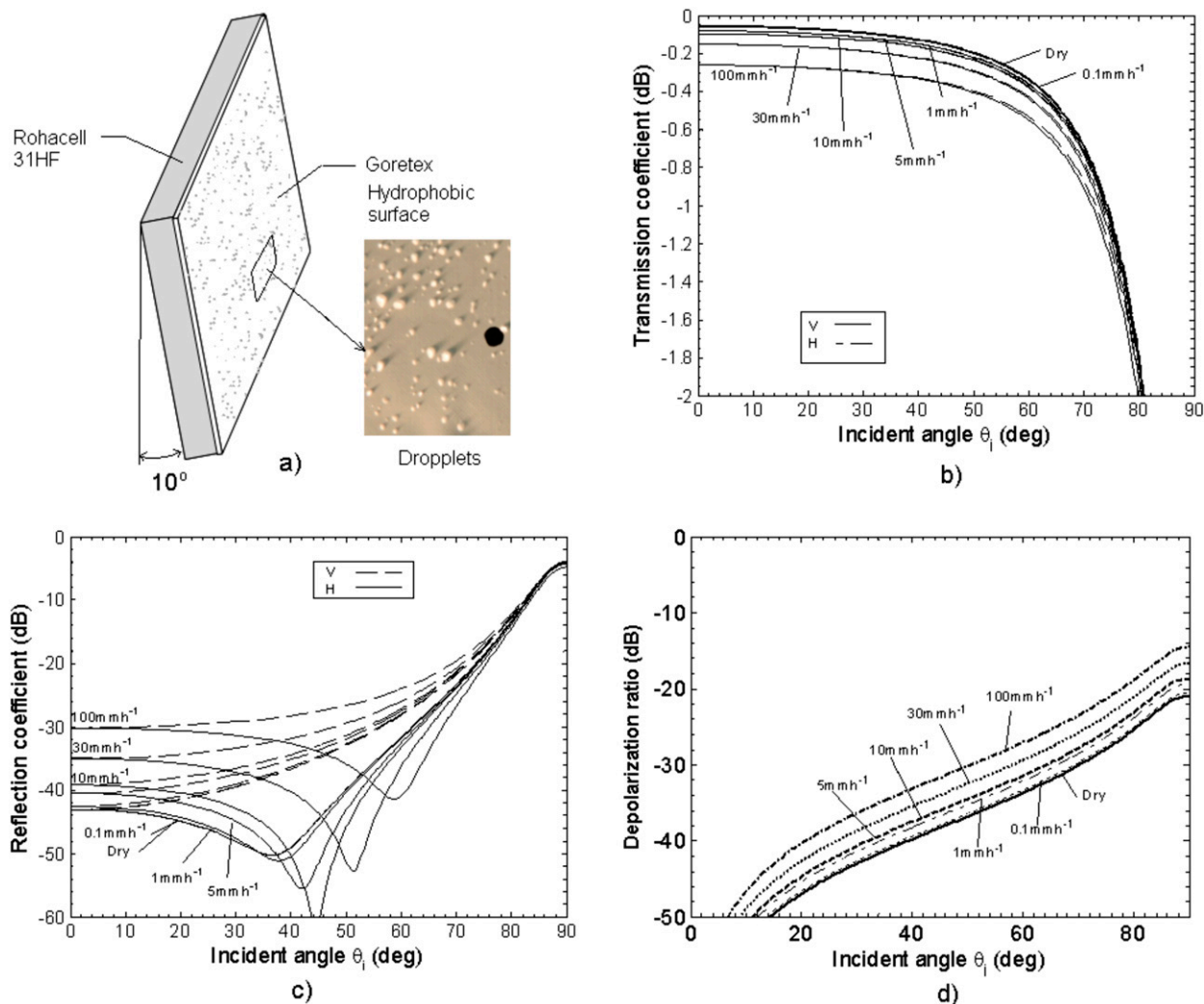
FIG. 20. Calculated results of hydrophobic (Gore-Tex) wet radome surface tilted (10°) under different rain intensities (0.1, 1, 5, 10, 30, and 100 mm h^{-1}): (a) transmission coefficient vs incident angle, (b) reflection coefficient vs incident angle, and (c) depolarization ratio vs incident angle.

Instead, a numerical model using the full-wave solver Ansys/Ansoft High-Frequency Structural Simulator (HFSS) is used. The HFSS model consists of a unit cell of 17 mm × 17 mm, where the droplets and rivulets were introduced as shown in Fig. 21b. Two models were considered: the first one represents the radome with droplets, and in the second one we add one rivulet to the unit cell. The results presented in Figs. 21c,d show that the transmission and reflection coefficients versus incident angle relation change drastically for both polarizations and change with incident angle. These preliminary results are important considering that the differences between H and V (due to the presence of rivulets in random fashion) can affect the performance of the radar system when it operates under rainy conditions.

Simulation results of the radome without the droplets were included in order to demonstrate the transmission lines circuital model proposed.

6. Summary

This paper presents a new analytical model developed to evaluate the performance of a wet radome of dual-polarized radar. The model requires a rain DSD model or reflectivity radar data and the geometry of radar radome as input parameters. The model proposed can be used for any radome type. A rectangular tilted unit cell was considered to discretize any radome shape (e.g., flat, spherical, semispherical, and conical radome). Then a projection of the rain drop size distribution in the tilted
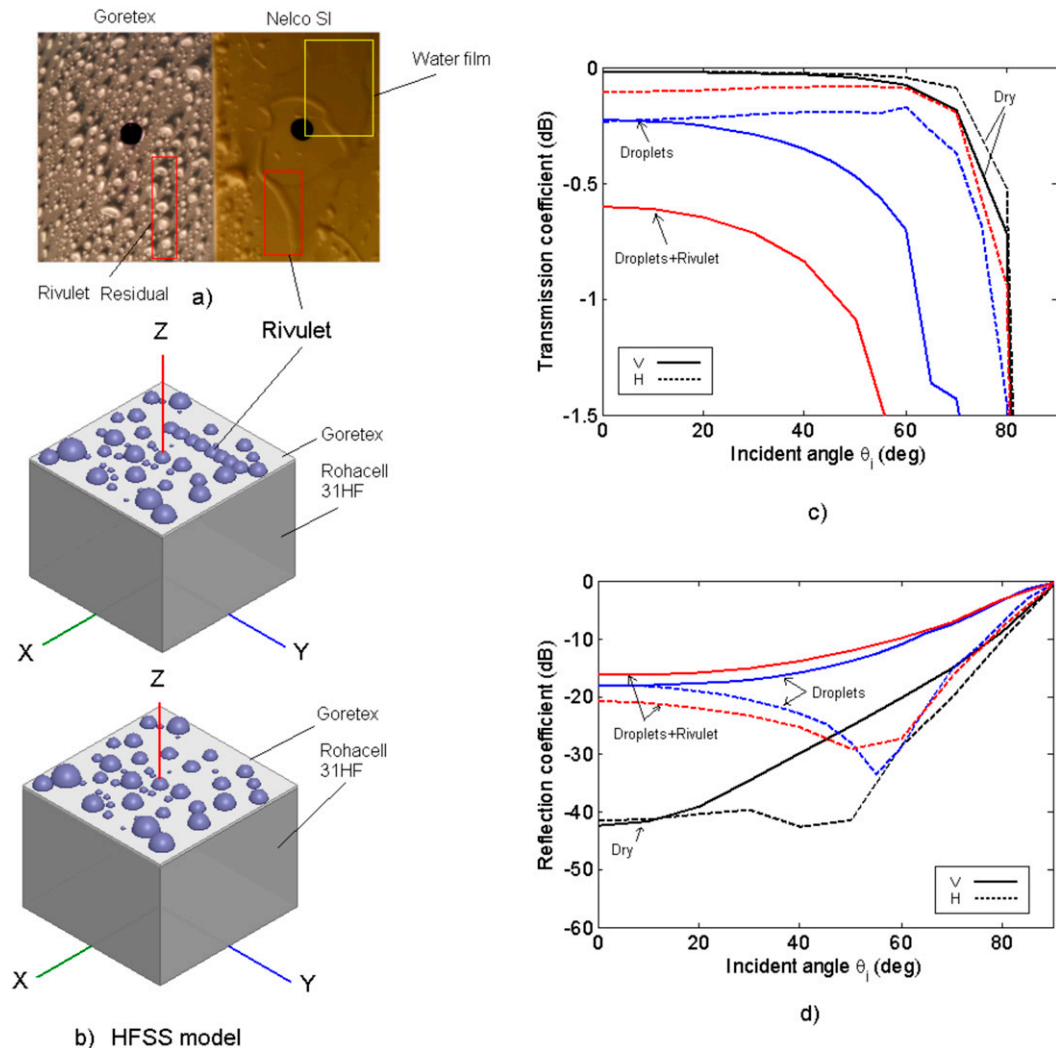
FIG. 21. Numerical simulation results of wet radome surface (hydrophobic) with and without the rivulets formation: (a) picture of water formation in a radome surface, (b) HFSS model for wet radome with and without rivulet formation, and (c),(d) simulated results of transmission and reflection coefficients.

unit cell was estimated. To consider the dynamic of the droplets based on the skin material (nonhydrophobic, hydrophobic, and superhydrophobic) and inclination, a formulation that estimates the angle when the droplet gravity is defeated by the drop surface tension was incorporated. This formulation takes into account the mechanical properties of the surface skin material and water. With the new projected drop size distribution in the radome surface (unit cell), an effective dielectric constant based on the mixing formulation was estimated based on the fractional volume between water and air. Having characterized the equivalent wet radome layer, the last part of the proposed model consisted of estimating the attenuation, reflecting, and depolarization of the wet layer and multilayer radome structure using a transmission line model. The proposed model does not

consider the turbulence in the air and also did not consider the rivulet formation.

A preliminary analysis of rivulets formation has also been discussed. Rivulet formation on a hydrophobic surface starts when the gravity force is larger than the surface tension of a large drop on the radome. When this happens, the drop runs and creates a vertical pattern with small droplets. Equation (8) can be used to estimate the number of rivulets on a flat tilted radome surface. The positions of the rivulets are random and the rivulet also depends on the tilt angle, surface material, and rainfall rate. Since rivulets present a vertical pattern, they affect vertical polarization more than horizontal polarization. This can be a problem for a polarimetric radar, since larger errors can be produced in the V channel and not necessarily in the H channel. To demonstrate the effect of

rivulets, a wet radome surface with droplets and rivulets was modeled in HFSS. For this specific example, the results at 45° (in azimuth) show that with the presence of rivulets in the radome surface, the attenuation in V is 0.8 dB, while without rivulets it is only 0.2 dB.

Using hydrophobic surfaces is the most successful approach for minimizing the water accumulation and preventing high attenuation, depolarization, and reflections. Unfortunately, hydrophobic surfaces are delicate and can easily lose their hydrophobic properties with a simple touch, dirt, pollution, rain erosion, and/or UV rays. The most durable hydrophobic surface maintains an acceptable hysteresis angle for 3–9 months. After that, the hydrophobicity needs to be replaced or repainted. A flat tilted radome surface has the flexibility to minimize water accumulation with a tilting angle. For example, reducing the tilting angle of a flat radome (based on Rohacell and Gore-Tex) from 34° to 10°, the results indicate a significant improvement in the radome performance. For a rainfall rate of 100 mm h^{-1} and an incident angle of 45° (in azimuth) and the radome tilted 34° (in elevation), the wet radome presents an attenuation of −1.3 dB (one way), a reflection of −17 dB, and a depolarization ratio of −25 dB. However, when the same radome is tilted only 10° (in elevation) and the attenuation is reduced to −0.38 dB (one way), the reflection is reduced to −28 dB and the depolarization ratio is reduced to −31 dB.

REFERENCES

Anderson, I., 1975: Measurements of 20-GHz transmission through a radome in rain. *IEEE Trans. Antennas Propag.,* **23,** 619–622, doi:10.1109/TAP.1975.1141134.

Bechini, R., V. Chandrasekar, R. Cremonini, and S. Lim, 2010: Radome attenuation at X-band radar operations. *Proc. Sixth European Conf. on Radar in Meteorology and Hydrology,* Sibiu, Romania, ERAD, P15.1. [Available online at http://www.erad2010.org/pdf/POSTER/Thursday/02_Xband/01_ERAD2010_0346_extended.pdf.]

Blevis, B., 1965: Losses due to rain on radomes and antenna reflecting surfaces. *IEEE Trans. Antennas Propag.,* **13,** 175–176, doi:10.1109/TAP.1965.1138384.

Bringi, V. N., and V. Chandrasekar, 2001: *Polarimetric Doppler Weather Radar: Principles and Applications.* Cambridge University Press, 494 pp.

Chang, K.-C., 1985: System performance in rain in a radome-enclosed environment. *1985 IEEE Military Communications Conference: MILCOM '85,* Vol. 1, IEEE, 293–299.

Clough, N. E., 2009: Innovations in ePTFE fiber technology: New capabilities, new applications, new opportunities. *Techtextil North America Symp. 2009,* Las Vegas, NV, Messe Frankfurt, 16 pp. [Available online at http://www.gore.com/MungoBlobs/168/901/ePTFE_INNOVATIONS_PAPER.pdf.]

Cohen, A., and A. Smolski, 1966: The effect of rain on satellite communications earth terminal rigid radomes. *Microwave J.,* **9,** 111–121.

Coulson, J. M., J. F. Richardson, J. R. Backhurst, and J. H. Harker, 1999: *Fluid Flow, Heat Transfer and Mass Transfer.* Vol. 1, *Chemical Engineering,* 6th ed. Butterworth Heinemann, 928 pp.

Crane, R. K., 2002: Analysis of the effects of water on the ACTS propagation terminal antenna. *IEEE Trans. Antennas Propag.,* **50,** 954–965, doi:10.1109/TAP.2002.800701.

Doviak, R. J., and D. S. Zrnić, 1993: *Doppler Radar and Weather Observations.* Academic Press, 562 pp.

Effenberger, J. A., R. R. Strickland, and E. B. Joy, 1986: The effects of rain on a radome's performance. *Microwave J.,* **29,** 261–274.

Fenn, A. J., 1997: Measurements of wet radome transmission loss and depolarization effects in simulated rain at 20 GHz. *10th International Conference on Antennas and Propagation,* Vol. 1, IEEE Conf. Publ. 436, 474–477.

Frasier, S. J., F. Kabeche, J. Figueras i Ventura, H. Al-Sakka, P. Tabary, J. Beck, and O. Bousquet, 2013: In-place estimation of wet radome attenuation at X band. *J. Atmos. Oceanic Technol.,* **30,** 917–928, doi:10.1175/JTECH-D-12-00148.1.

Frech, M., 2009: The effect of a wet radome on dualpol data quality. *34th Conf. on Radar Meteorology,* Williamsburg, VA, Amer. Meteor. Soc., P13.15. [Available online at https://ams.confex.com/ams/34Radar/techprogram/paper_155405.htm.]

——, B. Lange, T. Mammen, J. Seltmann, C. Morehead, and J. Rowan, 2013: Influence of a radome on antenna performance. *J. Atmos. Oceanic Technol.,* **30,** 313–324, doi:10.1175/JTECH-D-12-00033.1.

Gibble, D., 1964: Effect of rain on transmission performance of a satellite communication system. *IEEE International Convention Record, Part VI,* IEEE, 52.

Gorgucci, E., G. Scarchilli, and V. Chandrasekar, 1992: Calibration of radars using polarimetric techniques. *IEEE Trans. Geosci. Remote Sens.,* **30,** 853–858, doi:10.1109/36.175319.

——, R. Bechini, L. Baldini, R. Cremonini, and V. Chandrasekar, 2013: The influence of antenna radome on weather radar calibration and its real-time assessment. *J. Atmos. Oceanic Technol.,* **30,** 676–689, doi:10.1175/JTECH-D-12-00071.1.

Hendrix, C. E., J. E. McNally, and R. A. Monzingo, 1989: Depolarization and attenuation effects of radomes at 20 GHz. *IEEE Trans. Antennas Propag.,* **37,** 320–328, doi:10.1109/8.18728.

Hirsch, H. L., and D. C. Grove, 1988: *Practical Simulation of Radar Antennas and Radomes.* Artech House Antenna Library Series, Artech House, 304 pp.

Junyent, F., V. Chandrasekar, D. McLaughlin, E. Insanic, and N. Bharadwaj, 2010: The CASA Integrated Project 1 networked radar system. *J. Atmos. Oceanic Technol.,* **27,** 61–78, doi:10.1175/2009JTECHA1296.1.

Kurri, M., and A. Huuskonen, 2008: Measurements of the transmission loss of a radome at different rain intensities. *J. Atmos. Oceanic Technol.,* **25,** 1590–1599, doi:10.1175/2008JTECHA1056.1.

Lam, H., J. Din, L. Luini, A. D. Panagopoulos, and C. Capsoni, 2011: Analysis of raindrop size distribution characteristics in Malaysia for rain attenuation prediction. *2011 XXXth URSI General Assembly and Scientific Symp.,* Istanbul, Turkey, IEEE, 4 pp., doi:10.1109/URSIGASS.2011.6050806.

Manz, A., L. Handwerker, M. Löffler-Mang, R. Hannesen, and H. Gysi, 1999: Radome influence on weather radar systems with emphasis to rain effects. Preprints, *29th Int. Conf. on Radar Meteorology,* Montreal, Québec, Canada, Amer. Meteor. Soc., 918–921.

Merceret, F. J., and J. G. Ward, 2002: Attenuation of weather radar signals due to wetting of the radome by rainwater or incomplete filling of the beam volume. NASA Tech. Memo. NASA/TM—2002-211171, 16 pp. [Available online at http://ntrs.nasa.gov/archive/nasa/casi.ntrs.nasa.gov/20020043890.pdf.]

Nilsson, M. A., and J. P. Rothstein, 2012: Using sharp transition in contact angle hysteresis to move, defect, and sort droplets on a super hydrophobic surface. *Phys. Fluids,* **24,** 062001, doi:10.1063/1.4723866.

Rudge, A. W., K. Milne, A. D. Olver, and P. Knight, Eds., 1982: The Handbook of Antenna Design. Vol. 1, IEE Electromagnetic Waves Series, Vol. 15, Institution of Electrical Engineers, 710 pp.

Sas, L., R. E. Gorga, J. A. Joines, and K. A. Thoney, 2012: Literature review of supehidrophobic self-cleaning surfaces produced by electrospining. *J. Polym. Sci.,* **50B,** 824–845, doi:10.1002/polb.23070.

SCAT, 2009: Report of the investigation of models for evaluating technology to reduce attenuation in radomes for 9-GHz-band meteorological radars. Support Center for Advanced Telecommunications Technology Research.

Schneebeli, M., J. Sakuragi, T. Biscaro, C. F. Angelis, I. Carvalho da Costa, C. Morales, L. Baldini, and L. A. T. Machado, 2012: Polarimetric X-band weather radar measurements in the tropics: Radome and rain attenuation correction. *Atmos. Meas. Tech.,* **5,** 2183–2199, doi:10.5194/amt-5-2183-2012.

Sihvola, A., 2000: Mixing rules with complex dielectric co-efficients. *Subsurf. Sens. Technol. Appl.*, **1,** 393–415, doi:10.1023/A:1026511515005.

Thompson, R., A. Illingworth, and J. Ovens, 2012: Emission: A simple new technique to correct rainfall estimates from attenuation due to both the radome and heavy rainfall. *Weather Radar and Hydrology,* R. J. Moore, S. J. Cole, and A. J. Illingworth, Eds., IAHS Publ. 351, 39–44.

Trabal, J. M., I. Zawadski, and D. J. McLaughlin, 2008: A method to correct for wet radome attenuation in CASA radars by the use of a contiguous WSR-88D radar. *Proc. Fifth European Conf. on Radar in Meteorology and Hydrology,* Helsinki, Finland, ERAD, 0287.

Walton, J. D., Jr., 1970: *Radome Engineering Handbook: Design and Principles.* Marcel Dekker, Inc., 169–175.

Weigand, R. M., 1973: Performance of a water-repellent radome coating in an airport surveillance radar. *Proc. IEEE,* **61,** 1167–1168, doi:10.1109/PROC.1973.9238.

Zhang, G., J. Vivekanandan, and E. Brandes, 2001: A method for estimating rain rate and drop size distribution from polarimetric radar measurements. *IEEE Trans. Geosci. Remote Sens.,* **39,** 830–841, doi:10.1109/36.917906.